

Banner appropriate to article type will appear here in typeset article

# Submesoscale and boundary layer turbulence under mesoscale forcing in the upper ocean

**Shirui Peng<sup>1</sup>, Simone Silvestri<sup>2,1</sup> and Abigail Bodner<sup>1,3</sup>**

<sup>1</sup>Department of Earth, Atmospheric and Planetary Sciences, Massachusetts Institute of Technology, Cambridge, MA 02139, USA

<sup>2</sup>Department of Environment, Land and Infrastructure Engineering, Politecnico di Torino, Torino, Italy

<sup>3</sup>Department of Electrical Engineering and Computer Science, Massachusetts Institute of Technology, Cambridge, MA 02139, USA

**Corresponding author:** Abigail Bodner, abodner@mit.edu

(Received xx; revised xx; accepted xx)

---

The interaction among quasi-geostrophic mesoscale eddies, submesoscale fronts, and boundary layer turbulence (BLT) is a central problem in upper ocean dynamics. We investigate these multiscale dynamics using a novel large-eddy simulation on a 100 km-scale domain with meter-scale resolution. The simulation resolves BLT energized by uniform surface wind and convective forcing. A front interacts with BLT within a prescribed, spatially inhomogeneous mesoscale eddy field, representing a canonical eddy quadrupole. Using a triple flow decomposition, we analyze the dynamic coupling and kinetic energy budgets among the large-scale field, submesoscale field, and the resolved BLT. Our analysis reveals significant heterogeneity in the structure and intensity of submesoscales and BLT under varying mesoscale forcing. Turbulent kinetic energy and production rates can vary by an order of magnitude along the front, creating distinct turbulent hotspots whose locations are tied to the underlying large-scale flow. The region under stronger mesoscale convergence holds stronger horizontal and vertical geostrophic shear productions for BLT, and stronger self-production and BLT-destruction for submesoscales. In contrast, the region under dominant mesoscale divergence holds dramatic distortion of the front isotherm, along with dominant submesoscale vertical buoyancy production and self-destruction. These results provide a direct characterization of BLT and submesoscales in the ocean mixed layer modulated by a mesoscale eddy field, which can better inform future parameterization developments.

**Key words:** Authors should not enter keywords on the manuscript, as these must be chosen by the author during the online submission process and will then be added during the typesetting process (see [Keyword PDF](#) for the full list). Other classifications will be added at the same time.

## 1. Introduction

The upper ocean is a turbulent interface between the atmosphere and the deep ocean, a reservoir of dynamical processes across a vast range of scales (e.g., Ferrari & Wunsch 2009). At the largest scales, energy is injected by atmospheric winds and buoyancy fluxes and is organized into basin-scale gyres and mesoscale eddies, with typical scales of  $O(10\text{-}100)$  km. A portion of the energy is transferred towards smaller scales, notably into a vibrant field of submesoscale fronts and filaments ( $O(0.1\text{-}10)$  km), which can involve both upscale and downscale transfers, before its ultimate dissipation by microscale turbulence (e.g., McWilliams 2016; Taylor & Thompson 2023). The submesoscale is a dynamically critical regime where the influence of planetary rotation weakens, and ageostrophic, three-dimensional motions emerge, fundamentally controlling the vertical exchange of heat, carbon, and nutrients between the surface and the ocean interior (e.g., Lévy *et al.* 2012; Su *et al.* 2018; Boyd *et al.* 2019).

A central challenge in oceanic geophysical fluid dynamics is to understand and quantify the interaction between the largely balanced, quasi-geostrophic mesoscale flow and the fully three-dimensional, ageostrophic turbulence in the mixed layer (ML), the near-surface layer that is actively homogenized by atmospheric forcing. Submesoscale fronts, which are sharp, horizontal density gradients, serve as the natural laboratory for this problem. In the real ocean, ML temperature fronts can result from passing storm events, leaving abnormal horizontal ML gradients above a stratified interior. They can be energized by the strain field of the background mesoscale flow, which acts to sharpen the density gradients in a process known as frontogenesis (Hoskins & Bretherton 1972). Realistic simulations also discovered that ML temperature fronts can be strengthened by a balance known as Turbulent Thermal Wind (TTW) (Gula *et al.* 2014; Crowe & Taylor 2018). The frontogenetic evolution further triggers various instabilities, including symmetric, baroclinic, and shear instabilities. Symmetric and shear instabilities can drive intense turbulence and vertical mixing that arrest the frontal collapse, while baroclinic instabilities (BI) release the potential energy (PE) in the front and restratify the ML (Capet *et al.* 2008; Sullivan & McWilliams 2018).

Ocean fronts also interact constantly with boundary layer turbulence (BLT) driven by surface wind shear, convection, or waves (Thorpe 2005; McWilliams 2017). In particular, atmospheric wind and cooling can induce surface Ekman flow and convection, and their interactions with fronts can involve geostrophic shear production, Ekman buoyancy flux, or symmetric instability (e.g., Thomas 2005; Mahadevan *et al.* 2010; Thomas *et al.* 2013; Skillingstad *et al.* 2017; Callies & Ferrari 2018; Wenegrat 2023). These complex dynamics and mesoscale forcing collectively governs the momentum fluxes and energy budgets across scales within the ML. Therefore, comprehensively capturing their contributions in the ML relies on datasets that resolve a vast range of processes from the mesoscale down to meter-scale BLT. And understanding the different dynamical components requires analysis of the kinetic energy budgets, specifically to isolate and examine conversions between the submesoscale (SKE) and the turbulent (TKE) scales.

However, a persistent gap exists in modeling capabilities, leaving this multiscale interaction poorly constrained. Global ocean general circulation models are advancing towards resolving the mesoscale but must still parameterize the effects of both submesoscale features and BLT (Ferrari 2011; Bodner *et al.* 2023; Wagner *et al.* 2024; Silvestri *et al.* 2025). Regional hydrostatic models can successfully capture mesoscale-to-submesoscale transition. These simulations resolve how mesoscale strain generates sharp submesoscale fronts, in which frontogenesis drives a forward cascade of energy while BI a backward cascade (e.g. Srinivasan *et al.* 2023; Delpech *et al.* 2024). Yet, they lack the resolution

and non-hydrostatic physics required to explicitly represent BLT, relying instead on parameterizations that cannot capture the fine-scale structure of vertical transport, energy dissipation and their interactions with the larger scales. On the other hand, process-oriented Large Eddy Simulations (LES) have provided invaluable insight on submesoscale-BLT dynamics, such as Langmuir-submesoscale interactions, turbulence-induced frontogenesis and frontal arrest, etc (e.g., Hamlington *et al.* 2014; Skillingstad *et al.* 2017; Sullivan & McWilliams 2018; Verma *et al.* 2022; Bodner *et al.* 2023). These models explicitly resolve BLT but have historically relied on a critical idealization: the assumption of a spatially absent or uniform background mesoscale strain field.

The hydrostatic or uniform-strain assumption neglects the fundamental reality that these scale interactions are concurrent. While analytically and computationally convenient, idealizing the mesoscale forcing as uniform omits the intrinsic spatial heterogeneity of the real ocean and its effects that propagate onto the submesoscale to BLT transition. This simplification not only filters out the direct influence of mesoscale strain gradients but also neglects the critical role of mesoscale vorticity, which can hold wave modes and instabilities, such as vortex-Rossby waves (VRW) and inter-eddy edge waves, that can significantly alter frontal turbulence evolution (e.g., McWilliams *et al.* 2003; Dritschel & McIntyre 2008). In the real ocean, submesoscale fronts and eddies do not exist in isolation; they are continuously interacting with both the heterogeneous mesoscale background and BLT. This leaves a foundational question unanswered: how does the spatial heterogeneity of the mesoscale field modulate the structure, energetics, and turbulent properties along a submesoscale front? Answering this requires a simulation that can simultaneously resolve BLT while explicitly accounting for a non-uniform, large-scale mesoscale field.

In this study, we present results from a first-of-its-kind, large-domain LES that can resolve scales ranging from 100 km down to single meters (Fig. 1). The defining feature of this study is the imposition of a prescribed, time-invariant, and spatially inhomogeneous background velocity field,  $\mathbf{U}$ , which represents a canonical mesoscale eddy quadrupole. The LES resolves the perturbation velocity field  $\mathbf{u}$  evolving under the influence of this large-scale driver, as governed by the material derivative  $D/Dt = \partial/\partial t + (\mathbf{u} + \mathbf{U}) \cdot \nabla$ . This configuration couples a BLT-resolving LES with a persistent, non-uniform mesoscale field, allowing us to directly investigate the dynamic response of the front to a spatially varying environment. To distinguish various components in this multiscale system, we develop and apply a triple flow decomposition to quantitatively isolate the energetics of the large-scale, the submesoscale turbulence, and BLT.

By decomposing the flow into its prescribed mesoscale, along-front mean, filtered submesoscale, and BLT components, we quantify the dynamical coupling and kinetic energy budgets across scales. We demonstrate that the along-front structure of BLT is profoundly modulated by the mesoscale field, with local turbulent kinetic energy and production rates varying by an order of magnitude in response to heterogeneous background mesoscale and Ekman flow. This paper is structured as follows. §2 details the LES configuration, and §3 the triple decomposition methodology. §4 and §5 presents the primary results, focusing on the spatially varying structure of the front, its associated turbulence, and the multiscale energy budgets. In §6, we discuss the implications for vertical transport and submesoscale parameterization and summarize our key conclusions.

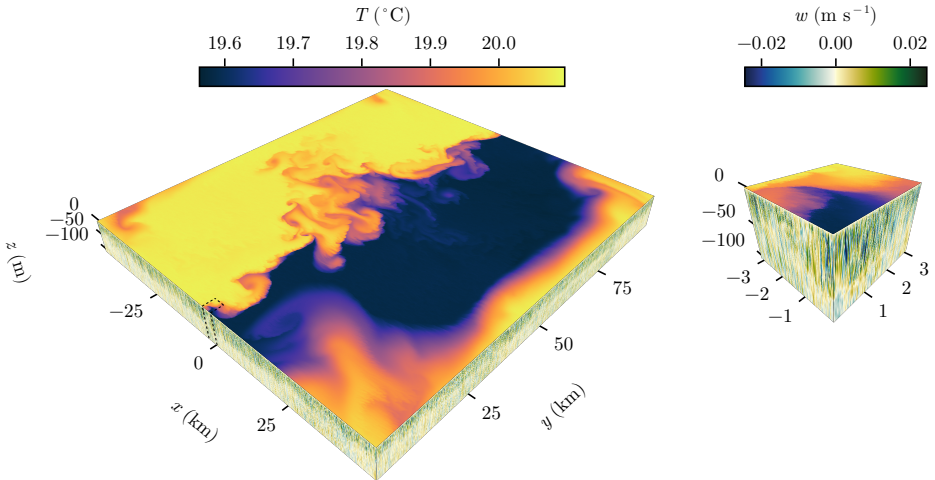


Figure 1. Visualization of surface temperature field  $T$  and cross-section vertical velocity field  $w$  in the computational domain above  $z = -100$  m at 7.5 d. Structures at multiple scales are developing in the visible horizontal plane (left), indicative of efficient energy transfer across scales. At the same time, 3D instability patterns and small-scale features are detectable in both horizontal and vertical cuts of the zoomed-in simulation domain (right), suggesting a forward turbulent cascade.

## 2. Numerical simulation

The simulation presented in this paper is of a frontal spin down in a rotating, incompressible Boussinesq fluid. The governing equations for momentum, temperature, and mass are

$$\frac{D\mathbf{u}}{Dt} + f\hat{z} \times \mathbf{u} = -\nabla\varphi + b\hat{z} + \mathbf{F}_u, \quad (2.1a)$$

$$\frac{DT}{Dt} = F_T, \quad (2.1b)$$

$$\nabla \cdot \mathbf{u} = 0, \quad (2.1c)$$

where

$$\frac{D}{Dt} = \frac{\partial}{\partial t} + (\mathbf{u} + \mathbf{U}) \cdot \nabla = \frac{\partial}{\partial t} + (u + U) \frac{\partial}{\partial x} + (v + V) \frac{\partial}{\partial y} + w \frac{\partial}{\partial z} \quad (2.2)$$

is the Lagrangian derivative with  $\mathbf{U} \equiv U\hat{x} + V\hat{y}$  a fixed background eddy strain field defined in Appendix A,  $f = 1 \times 10^{-4} \text{ s}^{-1}$  the Coriolis parameter at around 45° N,  $\varphi$  the geopotential, and  $b \equiv -g(\rho/\rho_0 - 1) = \alpha g T$  is seawater buoyancy relative to a reference density  $\rho_0 = 1020 \text{ kg m}^{-3}$ ,  $\alpha = 2 \times 10^{-4} \text{ }^{\circ}\text{C}^{-1}$  the thermal expansion coefficient,  $g = 9.81 \text{ m s}^{-2}$  the gravitational acceleration, and  $T$  is temperature. Velocity and temperature surface forcing terms are  $\mathbf{F}_u$  and  $F_T$ , respectively. Note that density is only affected by temperature here for simplicity. The equation set (2.1) is integrated using Oceananigans, a Julia package for simulation of incompressible fluid flows in an oceanic context (Wagner *et al.* 2025). The grid size is  $(N_x, N_y, N_z) = (20480, 20480, 224)$  and the simulation domain is  $(x, y) \in [0, L_x] \times [0, L_y]$ , where  $L_x = L_y = 100 \text{ km}$ , and  $z \in [-L_z, 0]$ , where  $L_z = 252 \text{ m}$ . The grid spacing is  $\Delta h = 4.88 \text{ m}$  and  $\Delta z = 1.125 \text{ m}$  in the horizontal and vertical directions, respectively. The resolution is close to that used in Hamlington *et al.* (2014) that resolves specific BLT-submesoscale interactions, although this model uses finite volume methods for horizontal derivatives instead of spectral derivatives as in Hamlington *et al.* (2014). This domain is partitioned into 1024 GPUs, which divide each

horizontal dimension uniformly into 32 ranks. In comparison, a hydrostatic version of the simulation can run on 1 GPU with  $\Delta h = 156.25$  m (Silvestri *et al.* 2025).

The domain is periodic in both horizontal directions. In the vertical, boundary conditions include momentum and temperature fluxes induced by a constant wind stress  $\tau$  and a uniform vertical temperature flux  $J^T$  at the top surface as

$$\mathbf{F}_u = -\frac{d[\tau\delta(z)]}{dz} = -\frac{\tau_w (\cos \theta \hat{x} + \sin \theta \hat{y}) \delta'(z)}{\rho_0}, \quad F_T = -\frac{d[J^T \delta(z)]}{dz} = \frac{Q \delta'(z)}{\rho_0 c_p}, \quad (2.3)$$

where  $|\tau| = \tau_w = 0.1 \text{ N m}^{-2}$  is the wind stress magnitude,  $\delta(z)$  a delta function concentrate at  $z = 0$ ,  $\theta = 30^\circ$  the wind angle,  $Q = 40 \text{ W m}^{-2}$  the surface heat flux out of the ocean (positive for cooling), and  $c_p = 3995 \text{ J K}^{-1} \text{ kg}^{-1}$  the heat capacity of seawater. The surface also has a flat condition  $w = 0$ . And at  $z = -L_z$  the conditions are initialized as no-flux,  $\partial u / \partial z = \partial v / \partial z = w = 0$ , and  $\alpha g \partial T / \partial z = 0.1 N_T^2$ , where  $N_T^2 = 2 \times 10^{-4} \text{ s}^{-2}$  is a deep pycnocline water buoyancy frequency squared.

The prescribed background eddy velocity field  $\mathbf{U}$  represents four stationary and near-barotropic mesoscale eddies arranged in a quadruple pattern (Fig. 2ab). The setup is a combination of that in Hamlington *et al.* (2014) without Stokes components and the one in Thomas & Ferrari (2008) with strain. The eddies have a radius at  $R = L_x/4 = 25$  km, a surface-level anomaly magnitude at  $\Phi = 0.01$  m, and a vertical temperature profile that is constant in the ML and decreases by  $\Delta T^e = 0.1^\circ\text{C}$  at the bottom. To represent the eddy effect on the isopycnal, the depth below which the temperature starts decreasing is slightly deeper(shallower) for warm(cold)-core eddies, with a difference of  $\Delta m = 30$  m. The eddy velocities consist of a dominant barotropic part corresponding to the surface-level anomaly and a mild baroclinic part related to the vertical temperature profile. The velocity has a maximum of  $0.058 \text{ m s}^{-1}$  in the surface layer and decreases slightly at the bottom. This background field acts as an idealized mesoscale advection of temperature and momentum, while the eddy temperature  $T_M$  is superimposed onto the background stratification as part of the initial condition. We assume the eddies are fixed in the ML throughout the simulation duration.

The initial state of the simulation is a temperature profile  $T_i(x, y, z) = T_M(x, y, z) + T_0(x, z)$ , and a jet  $\mathbf{u}_i = v_0(x, z) \hat{y}$  in thermal wind balance with  $b_0 = \alpha g T_0$  as

$$v_0 = \frac{1}{f} \int_{-\infty}^z \frac{\partial b_0}{\partial x} dz. \quad (2.4)$$

Here  $T_M$  is also in thermal wind balance with  $\mathbf{U}$ . We initialize  $T_0$  as a two-front configuration (Fig. 2bc) (Hamlington *et al.* 2014; Verma *et al.* 2022). It consists of a weakly stratified surface layer above a strongly stratified thermocline and a moderately stratified lower layer. The analytical form of  $v_0$  and  $T_0$  is given in Appendix B. The initial condition results in two fronts oriented in the  $y$  direction, one located at  $x = 0$  km and one at  $x = 50$  km, where the buoyancy gradient at each front has a magnitude of  $M_0^2 = 5 \times 10^{-7} \text{ s}^{-2}$ . Due to the periodicity of the domain and the imposed wind stress as described below, one front remains stable, whereas instabilities form along the other under both mesoscale forcing and Ekman buoyancy flux, an important mechanism for generating submesoscale activity (Thomas 2005; Thomas *et al.* 2013; Skillingstad *et al.* 2017). The mean mixed-layer depth (MLD) is  $m_0 = 60$  m with an initial squared Brunt–Väisälä frequency  $N_s^2 = 5 \times 10^{-7} \text{ s}^{-2}$ , representative of the MLD in the western boundary current regions during October to December (Treguier *et al.* 2023). We set a transition layer with a depth of  $\Delta m^f = 10$  m between the ML base and the pycnocline. The pycnocline stratification is characterized by  $N_T^2$  between 70 to 100 m depth, below which the stratification is reduced by a factor of 10.

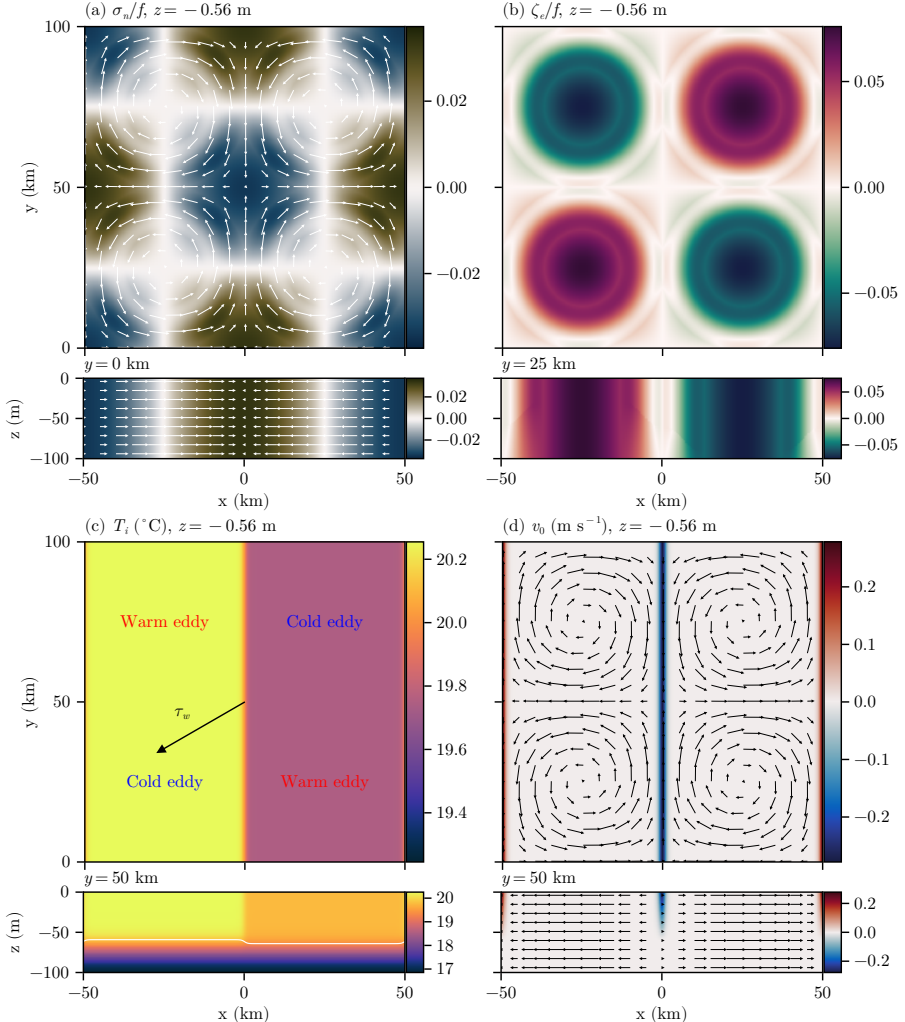


Figure 2. Snapshots of (a) background mesoscale strain rate  $\sigma_n = -\frac{1}{2}(\partial U/\partial x - \partial V/\partial y) = -\partial U/\partial x$ , (b) background mesoscale vorticity  $\zeta_e = \partial V/\partial x - \partial U/\partial y$ , (c) initial temperature  $T_i$ , and (d) initial jet velocity  $v_0$ . The  $x - y$  slices are at  $z = 0.56$  m, and the  $x - z$  slices are at  $y = 0$  km for (a),  $y = 25$  km for (b), and  $y = 50$  km for (c,d). Arrows in (a,d) indicate velocity vectors of the eddy forcing. The black arrow in (a) indicates the wind direction. White lines in (a) show the initial mixed layer depth. Light rings in (b) that are roughly at a half radius point implies merged effects due to compactly positioned eddy quadruple.

We designed the stratification and surface forcing to ensure a representative and relatively stable evolution of the MLD (Legay *et al.* 2024). Following the framework of Legay *et al.* (2024), we plot the initial horizontal distribution of four dimensionless parameters that characterize ML dynamics (Fig. 14). The parameter  $\lambda_s = -B_0 h/u_*^3$  represents the relative contribution of surface cooling and wind forcing, where  $B_0 = -Q/(\rho_0 c_p \alpha g)$  is the buoyancy flux,  $h$  is the MLD computed based on a buoyancy difference of  $3 \times 10^{-4}$  m s<sup>-2</sup> from the surface (Griffies *et al.* 2016), and  $u_* = \sqrt{\tau_w/\rho_0}$  is the friction velocity. The two Richardson numbers,  $R_h = (N_h h/u_*)^2$  and  $R_h^* = (N_h h/w_*)^2$ , describe the stability of the ML with respect to wind-driven turbulence and convective mixing, respectively. Here  $N_h^2$

represents the stratification at the base of the ML, and  $w_* = (-B_0 h)^{1/3}$  is the convective velocity scale. The last parameter,  $f/N_h$ , characterizes the influence of rotation relative to stratification.

Red regions in Fig. 14 indicate parameter values that fall within the 30 % highest-density contours in the global parameter space analyzed by Legay *et al.* (2024) (see their Fig. B1), which also broadly corresponds to conditions associated with stable MLD evolution (see their Fig. 2). Specifically,  $\lambda_s \gtrsim 10^{-0.6} \approx 0.25$  indicates  $B_0$  or convection, compared to  $u_*$  or wind shear, as the driving force of MLD deepening (Fig. 14a). And a pattern of  $R_h \gtrsim 10^3$  and  $R_h^* \gtrsim 10^{3.5} \approx 3 \times 10^3$  implies stable ML stratification under the given surface forcing (Fig. 14bd). Although these thresholds come from 1D results and vary with horizontal heterogeneity (Legay *et al.* 2024), we regard them as pragmatic dynamical bounds for the parameter choice. Notably, light color transitions in the plots coincide with the locations of submesoscale fronts and cold-core eddies, while warm-core eddies exhibit a weaker imprint. This difference likely arises because warm-core eddies deepen isopycnals, but their influence is masked by the stronger background stratification below the mean MLD.

### 3. Multiscale energetics

The spatially inhomogeneous nature of the background flow  $\mathbf{U}$  and the lack of time-averaged data necessitate a flow decomposition based on spatial filtering. We adopt the approach taken in Johnson & Fox-Kemper (2024) for a multi-level decomposition for the total velocity field

$$\mathbf{u}_{total} = \mathbf{U} + \mathbf{u} = \mathbf{U} + \bar{\mathbf{u}} + \mathbf{u}' = \mathbf{U} + \mathbf{u}^a + \mathbf{u}^s + \mathbf{u}', \quad (3.1)$$

where  $\bar{\mathbf{u}}$  represents a 2D horizontal Gaussian filter with a length scale of 300 m permitted as submesoscale (Hamlington *et al.* 2014; Bodner & Fox-Kemper 2020), and  $\mathbf{u}'$  are the finer-than-submesoscale fluctuations, representing BLT. When using the filtering for subdomains, we apply reflective boundary conditions for non-periodic boundaries and focus on results away from the boundaries. The next decomposition separate the frontal flow from the wind-driven Ekman flow by an along-front average in the  $y$  dimension  $\langle \bar{\mathbf{u}} \rangle = \mathbf{u}^a = \bar{\mathbf{u}} - \mathbf{u}^s$  (Johnson & Fox-Kemper 2024). Note that this along-front average still contains a mean frontal component besides the Ekman flow. In this framework, we will have advection of the large-scale along-front mean flow  $\mathbf{u}^a$ , despite suppressing that for the barotropic eddies in equation (2.1), with the assumption being that the mesoscale eddies are stationary within the time frame relevant for the simulation physics. For any variable  $\phi$ , we denote  $\overline{\mathbf{u}'\phi'} = \bar{\mathbf{u}}\phi - \bar{\mathbf{u}}\bar{\phi}$  (Germano 1992). We define the submesoscale kinetic energy,  $SKE \equiv \frac{1}{2}\mathbf{u}^s \cdot \mathbf{u}^s$  (Verma *et al.* 2022), and the turbulent kinetic energy (TKE) as  $TKE \equiv \frac{1}{2}(\overline{u'^2} + \overline{v'^2} + \overline{w'^2})$ .

### 4. Unstable front develops heterogeneous structures

In this study, we focus on a small subset of the simulation output, the unstable frontal region before its collapse, to ensure the analysis is computationally trackable. We explore the evolution of the simulation at later times in a follow up study. This region, between  $-12.5$  to  $12.5$  km in  $x$ , shows rich multiscale evolution in the along-front direction (Fig 3). We first characterize the flow in a qualitative overview of the front's structural evolution within the varying mesoscale eddy field.

The evolution of the surface vertical vorticity field highlights the frontal response to the heterogeneous mesoscale flow (Fig 3). Initially, the front is characterized by two parallel

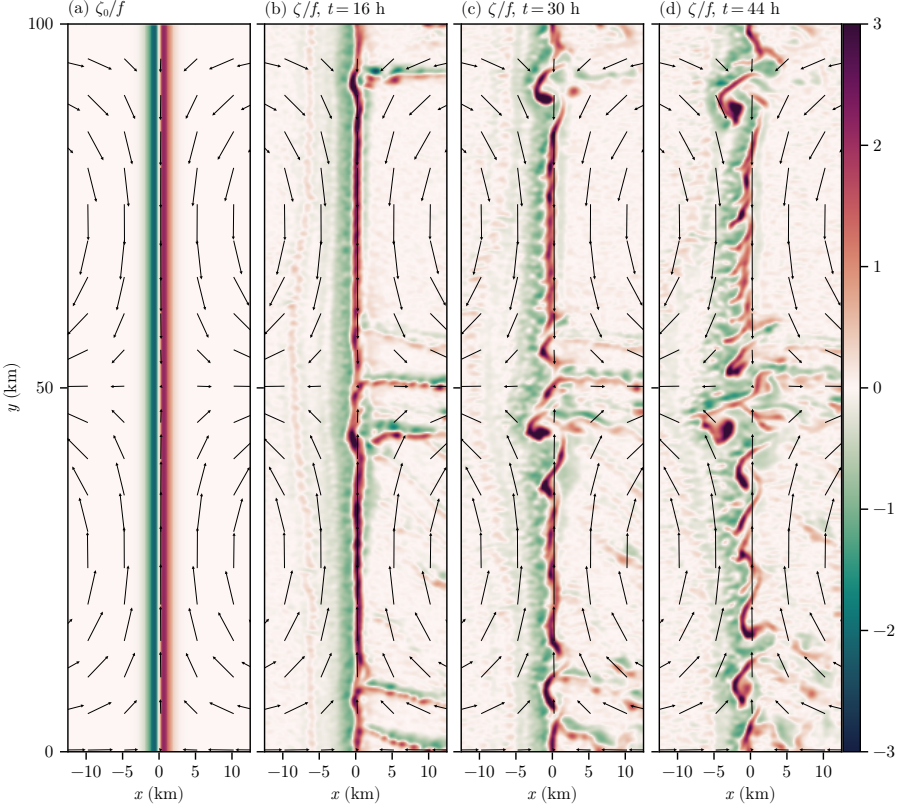


Figure 3. Snapshots of normalized surface vertical vorticity at (a) initialization, (b) 16 h, (c) 30 h, and (d) 44 h. The initial vorticity in (a) is calculated on a coarser grid with a horizontal spacing of 156.25 m. This grid is enough to resolve the initial frontal jet and is created with 1 GPU. We do not need filtering since no turbulence is initialized. While those in other panels are calculated on the meter-scale grid after a 300 m-Gaussian kernel smoothing. Arrows indicate velocity vectors of the eddy forcing.

bands of cyclonic ( $\zeta_0/f > 0$ ) and anticyclonic ( $\zeta_0/f < 0$ ) vorticity of equal magnitude, consistent with the thermal wind balance of the initial state (Fig 3a). By  $t = 16$  h, the cyclonic band sharpens and intensifies with significant local Rossby number  $\bar{\zeta}/f = O(1)$  (Fig 3b). Concurrently, two groups of enhanced vorticity band emerge for  $x \geq 0$ , one around  $y = 0$  and the other around  $y = 50$  km, corresponding to regions of background strain extremes. By  $t = 30$  h, these bands have triggered significant curvature on the along-front cyclonic band, and the two features slightly downstream of the strain extremes undergo severe meander (Fig 3c), signifying the growth of frontal BI. By  $t = 44$  h, the front has fragmented into a complex field of submesoscale eddies and filaments, indicating that instabilities have grown to a developed stage (Fig 3d). Consistent with the background mesoscale strain, the submesoscale features are more spread out in the diverging zone ( $y = 50$  km) than they are in the converging zone ( $y = 0$  and 100 km). Similar evolution also shows up in the surface divergence plot (Fig 15).

The qualitative evolution discussed above is quantified by tracking several frontal properties over time (Fig. 4). We use three surface temperature contours to define a consistent frontal region (Fig. 5a). Specifically, we first use the marching squares algorithm to find isolines of the spatially-smoothed surface temperature  $\bar{T}_{\text{surf}}$ . We then select those

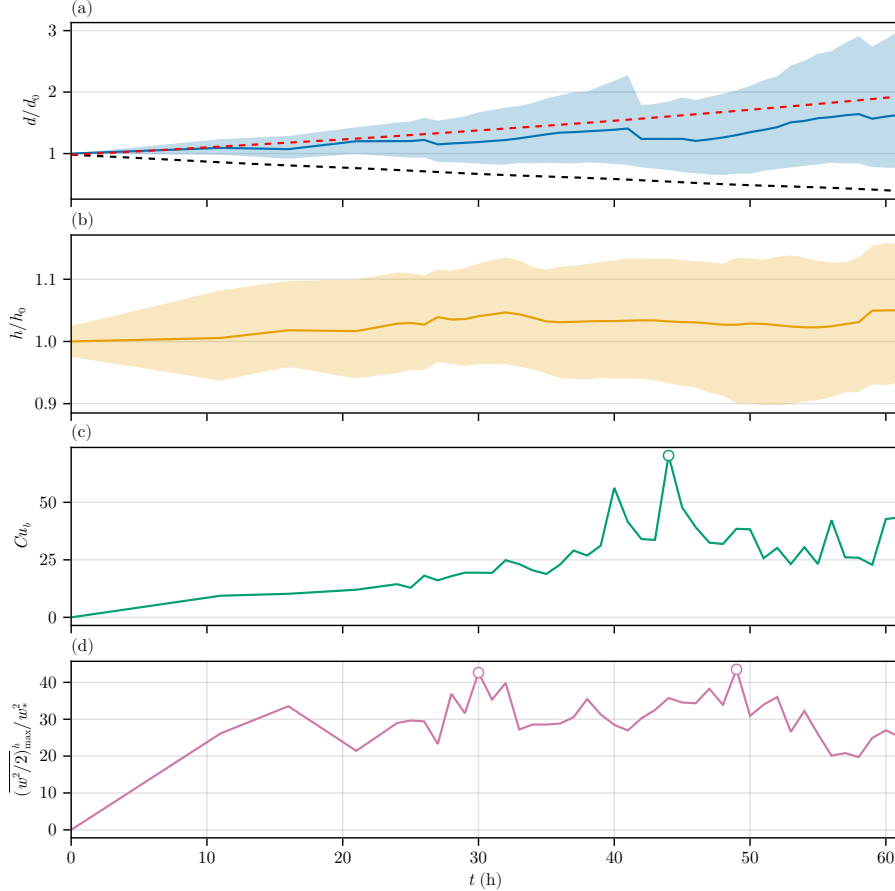


Figure 4. Time evolution for (a) mean frontal width  $d$  normalized by  $d_0 = 2$  km, (b) mean mixed layer depth  $h$  in the front region normalized by  $h_0 = 60$  m, (c) bulk curvature number  $Cu_b$  along the central front isotherm, and (d) mixed-layer-averaged vertical kinetic energy maximum  $\overline{w^2/2}_{\text{max}}^h$  in the front region normalized by  $w_*^2$ . Shadings in (a)(b) illustrate the 10-th and 90-th percentile range, while circles in (c)(d) local peaks. Black and red curves in (a) are predictions from uniform strain frontogenesis theory (Shakespeare & Taylor 2013), with  $\sigma_n = \pm 0.03f$  for black and red, respectively. The bulk curvature number is the maximum along-front local curvature number  $Cu \equiv 2u_g\kappa/f$ , with  $u_g = \alpha g \Delta Th/fd$  the geostrophic velocity scale and  $\kappa$  the geometric curvature. Only solid lines of  $d$  and  $h$  are averaged over the whole frontal domain.

isotherms with small  $x$ -ranges  $x_{\text{max}} - x_{\text{min}} < 12.5$  km and large  $y$ -ranges  $y_{\text{max}} - y_{\text{min}} > 90$  km as frontal contour candidates. We identify the front's centre contour as the isoline of the mean temperature  $\bar{T}_{\text{front}}$  in this candidate set. Two additional isotherms  $\bar{T}_{\text{front}} \pm 0.194$  °C are then selected as frontal boundaries such that the initial frontal width is 2 km. We present analysis on the frontal width, MLD, bulk curvature number, and vertical kinetic energy. The bulk curvature number  $Cu_b$  is defined as the maximum value of the along-front curvature normalized by the geostrophic balance scale (Shakespeare 2016), giving the curvature number  $Cu \equiv 2u_g\kappa/f$ , with  $u_g = \alpha g \Delta Th/fd$  the geostrophic velocity scale and  $\kappa$  the geometric curvature.

Both the along-front mean and variation of normalized frontal width  $d/d_0$  and MLD  $h/h_0$  increase with time under yet different patterns and evolution dynamics (Fig. 4ab). We define  $d$  along the centre frontal contour as the sum of the smallest distances to the two

frontal boundaries. Here we compute  $h$  based on a density difference of  $0.09 \text{ kg m}^{-3}$  from  $z = -10 \text{ m}$ . This threshold is three times the conventional choice of  $0.03 \text{ kg m}^{-3}$  (Treguier *et al.* 2023), which can better capture the base of the ML under active multiscale processes (Epke *et al.* 2025). The 10-th and 90-th percentile bounds of  $d/d_0$  are strongly coupled to the heterogeneous strain field, as will be confirmed in the along-front analysis later. Compared to the frontogenesis theory proposed by Shakespeare & Taylor (2013) based on a constant strain  $\sigma/f = \pm 0.03$  close to the prescribed mesoscale extremes here, the 10-th percentile of  $d/d_0$  closely follows the prediction for converging strain up to about 50 h, while the 90-th percentile increases more rapidly than the theory with a constant diverging strain. This asymmetry suggests that processes apart from strain could be contributing significantly to widen the front. Here these dynamics could involve BLT-induced frontal arrest and diffusion and growth of submesoscale BI (Fig. 5).

For the normalized MLD  $h/h_0$ , the 10-th and 90-th percentiles likely reflect compound effects from initialization across-front differences, restratification, and mixing (Fig. 4a, 5ab). In particular, the finite percentile range at  $t = 0$  result from shallower versus deeper initialized MLD  $h$  for warmer and colder ML, respectively (Fig. 2c). The time evolution of  $h/h_0$  reveals a spatially and temporally variable interplay between BLT-driven deepening and submesoscale restratification (e.g. Capet *et al.* 2008; McWilliams 2016; Verma *et al.* 2022). The asymmetry here is weaker yet shows a slightly stronger increase in the 90-th percentile in the earlier stage, in contrast to a stronger 10-th percentile variability in the later stage after the bulk curvature number peak. This is consistent with faster BLT-deepening and slower submesoscale-restratification. We further provide direct, localized evidence for this coupling in the subsequent vertical cross-section analysis. Comparing the time series of  $d/d_0$  and  $h/h_0$  also indicates a more significant strain impact on the former based on the frontogenesis analysis.

The bulk curvature number  $Cu_b$  grows approximately linearly until about  $t \approx 30 \text{ h}$  (Fig. 4c). After this point, its growth accelerates dramatically, peaking around  $t = 44 \text{ h}$  as the front visibly fragments (Fig. 3c). The MLD-averaged vertical kinetic energy, a proxy for BLT intensity, exhibits a primary peak around  $t = 30 \text{ h}$  (Fig. 4d). This timing could suggest a transition from BLT-dominant early evolution to submesoscale-dominant instabilities which leads to a secondary peak in vertical kinetic energy around  $t = 48 \text{ h}$ . We focus this evolution analysis prior to  $t = 61 \text{ h}$ , after which the frontal fragmentation makes a coherent front-following analysis less reliable.

## 5. Multiscale interactions along the unstable front with changing strain

After identifying a dynamically representative time,  $t = 30 \text{ h}$ , we transition to a quantitative analysis in a front-following coordinate system. In this coordinate, we examine how properties such as the MLD, frontal width and curvature, TKE, and SKE vary along the frontal coordinate relative to the local mesoscale strain. This analysis is followed by a systematic comparison of various TKE and SKE budget terms across four vertical slices along the front. And the last subsection present a description of a secondary mesoscale-Ekman effect that we find to contribute to the early along-front heterogeneity.

### 5.1. Mesoscale forcing induces non-uniform turbulent coupling along the front

Based on the temporal evolution, we select  $t = 30 \text{ h}$  for a detailed investigation. It represents a mature frontal state with strong turbulent activity, immediately prior to the dominance of extreme frontal curvature and further developed instabilities. Horizontal slices at this time reveal an unstable front around  $x = 0$  holding various emerging perturbations (Fig. 5). Signatures of emerging meanders are visible in the surface temperature field  $T_{\text{surf}}$ ,

## Turbulent ocean front under strain

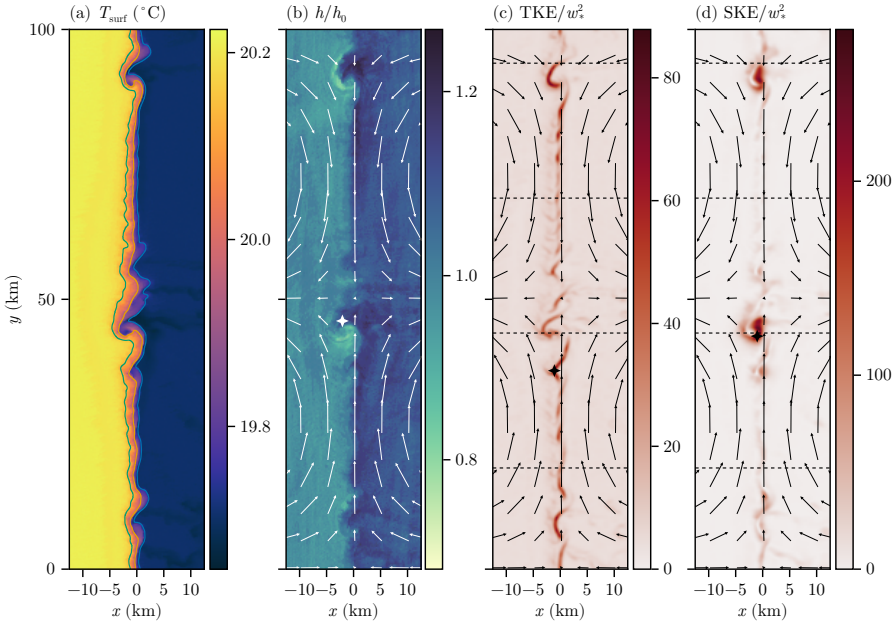


Figure 5. Horizontal slice of (a) surface temperature  $T_{\text{surf}}$ , (b) normalized mixed layer depth  $h/h_0$ , (c) normalized turbulent kinetic energy  $\text{TKE}/w_*^2$ , and (d) normalized submesoscale kinetic energy  $\text{SKE}/w_*^2$  at 30 h. The vertical level is  $z = -0.56$  m for TKE and  $z = -2.81$  m for SKE, which is based on where the maximum is located. The center contour in (a) corresponds to  $19.93$  °C, and the two boundary contours are offset by  $0.194$  °C which gives an initial frontal width of 2 km. Arrows in (b)-(d) shows the velocity vector field that induces the strain, while white and black stars the maximum of  $h$ -averaged vertical kinetic energy, near-surface TKE ( $z > -4.5$  m), and near-surface SKE ( $z > -4.5$  m), respectively. Four dashed lines in (c,d) show slice locations along  $y = 93.75$ ,  $68.75$ ,  $43.75$ , and  $18.75$  km to be discussed in §5.2.

particularly in the adjacent downstream regions of strong mesoscale strain (Fig. 5a). The MLD  $h/h_0$  remains generally deeper on the cold, dense side of the front, though localized shallowing is evident near the emerging meanders, suggesting restratification effect by submesoscale BI (Fig. 5b). Hotspots of normalized near-surface TKE are concentrated along the front (Fig. 5c), with its maximum located slightly further downstream from the ML-averaged vertical kinetic energy maximum (black star in Fig. 5c vs. white star in Fig. 5b). This difference is consistent with possibly deeper MLD at the TKE maximum location, compared to shallower MLD at the maximum location of ML-averaged  $\frac{1}{2}w^2$  under submesoscale restratification. In fact, the SKE maximum is nearly co-located with that of ML-averaged vertical kinetic energy. More generally, normalized near-surface SKE is concentrated into two strongest meandering modes near  $y = 44$  and  $93$  km, indicative of two emerging ML eddies due to submesoscale BI (Fig. 5d). Note that due to the removal of the along-front average in the multiscale decomposition §3 the SKE field in Fig. 5 reflects submesoscale instabilities that deviate from the mean frontal structure, such as BI and smaller fronts and filaments.

To investigate the influence of the mesoscale strain field, we project various quantities onto a coordinate system defined by the frontal arc length,  $s$  (Fig 6). We first resample the centre frontal contour into  $N = 10240$  points  $\{\mathbf{r}_i = (x_i, y_i)\}_{i=1}^N$  and compute cumulative sums of their interval lengths to get  $s$ . The normalized coordinate  $s/L_y$  is helpful to identify along-front locations relative to  $y$ . We define the instantaneous strain rate along the frontal coordinate normal  $\mathbf{n} = (n_x, n_y) \propto d^2\mathbf{r}/ds^2$  as  $S_n = -[n_x^2 \partial U / \partial x + n_y^2 \partial V / \partial y +$

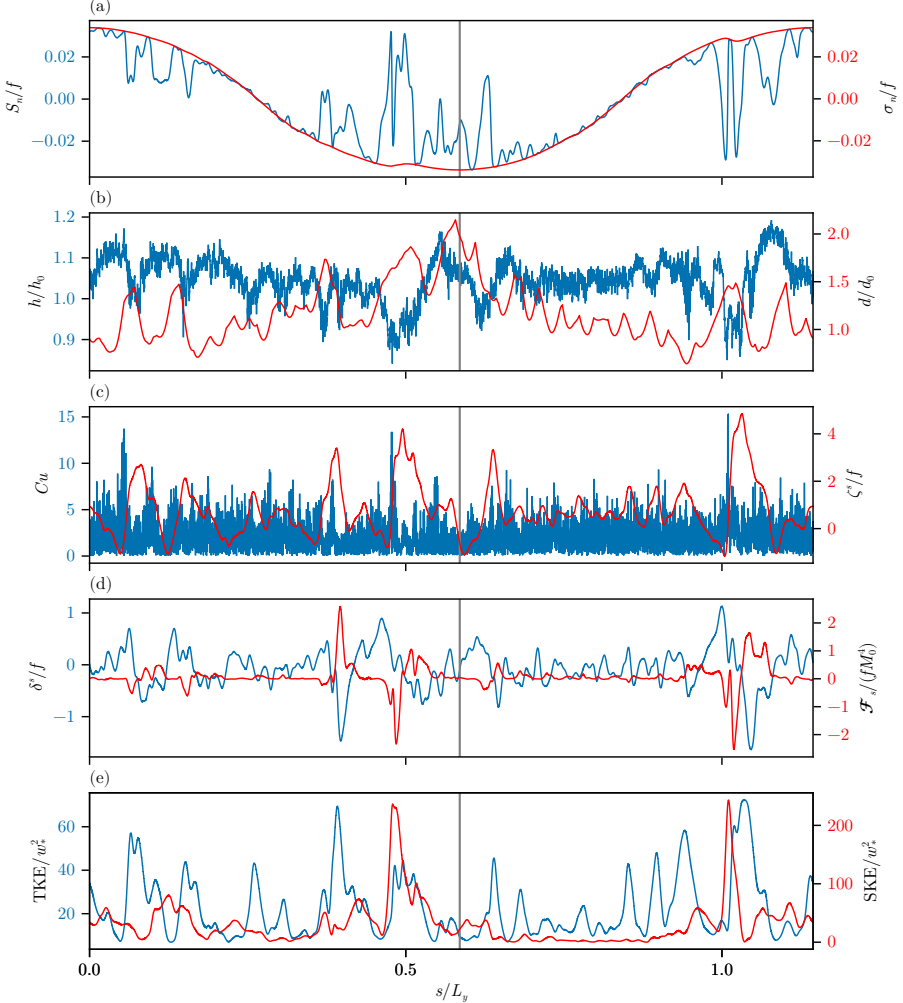


Figure 6. Along-front profiles of (a) surface frontal normal strain  $S_n/f$  and background strain  $\sigma_n/f$ , (b) surface frontal width  $d/d_0$  and mixed layer depth  $h/h_0$ , (c) local curvature number  $Cu$  and submesoscale vorticity  $\zeta^s/f = (v_x^s - u_y^s)/f$ , (d) submesoscale divergence  $\delta^s/f = (u_x^s + v_y^s)/f$  and frontogenetic tendency  $\mathcal{F}_s = -(b_x^s u_x^s + b_y^s v_y^s) - b_x^s b_y^s (u_y^s + v_x^s)$  normalized by  $f M_0^4$ , and (e) turbulent kinetic energy  $TKE/w_*^2$  and submesoscale kinetic energy  $SKE/w_*^2$ . All taken at 30 h and on the center contour of Fig. 5a. All submesoscale variables are computed on  $z = -2.81$  m. The grey vertical line denotes where  $\sigma_n/f$  reaches the strongest divergence (minimum).

$n_x n_y (\partial U / \partial y + \partial V / \partial x)$ . For other variables of interest, we interpolate the corresponding horizontal field onto  $\{\mathbf{r}_i\}_{i=1}^N$  using nearest-neighbor and periodic boundary condition.

The instantaneous normal strain  $S_n/f$  generally overlaps with the time-invariant normal strain  $\sigma_n/f = \frac{1}{2}(\partial U / \partial x - \partial V / \partial y)/f$  (Fig 6a blue vs. orange curves). The MLD  $h/h_0$  is reasonably noisy since its computation is based on the raw temperature field (Fig 6b). It tends shallower when there is significant strain perturbation around  $s/L_y = 0.5$  and 1.0, where submesoscale BI are located. The frontal width  $d/d_0$  shows a strong anti-correlation with  $\sigma_n/f$ : it is maximized with strain minimum and minimized with strain maximum, consistent with the front being physically stretched and compressed (Fig 6b, also 5a).

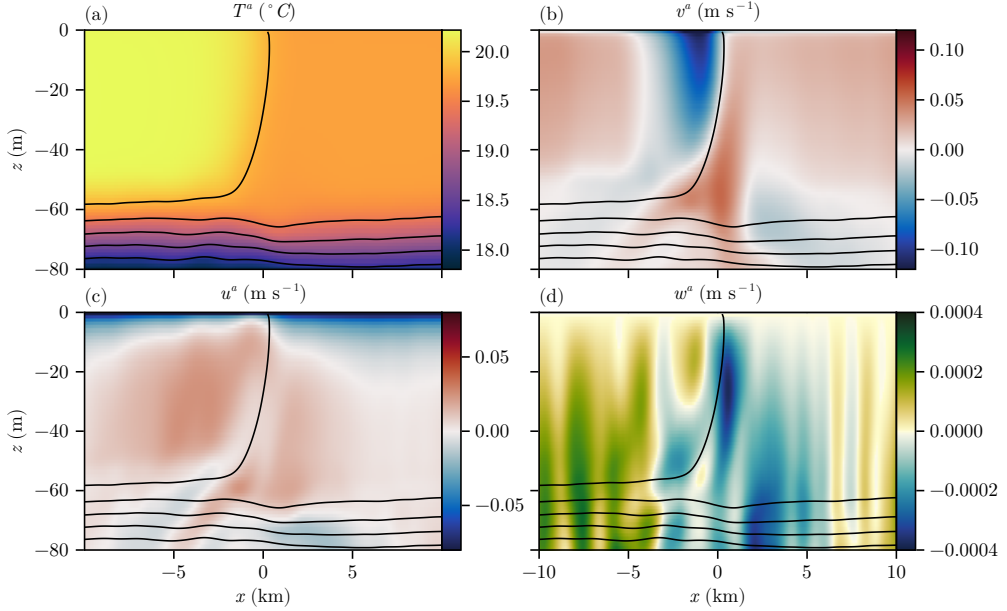


Figure 7. Along-front mean fields of (a) temperature  $T^a$ , (b) along-front velocity  $v^a$ , (c) across-front velocity  $u^a$ , and (d) vertical velocity  $w^a$  at 30 h.

Peaks in along-front local curvature number  $Cu = 2u_g\kappa/f$  are co-located with enhanced submesoscale vorticity  $\zeta^s = (v_x^s - u_y^s)/f$  (Fig 6c). Submesoscale divergence  $\delta^s = (u_x^s + v_y^s)/f$  reaches local minimum roughly with the local maximum of frontogenetic tendency  $\mathcal{F}_s = -(b_x^s u_x^s + b_y^s v_y^s) - b_x^s b_y^s (u_y^s + v_x^s)$ , although the former shows higher overall variability (Fig 6d). Similarly, TKE appear as random pulses with enhanced magnitude near strain extremes, while SKE is dominated by two maxima aligning with background strain extrema (Fig 6e). Two SKE peaks match two dips in  $\mathcal{F}_s$ , dynamically consistent with finite amplitude growth of BI. Although this along-front correlation analysis does not necessarily transfer to causal dynamics, we can better understand the local and instantaneous dynamics by examining contributions to TKE and SKE budgets across a few vertical sections with distinct background strain.

Since the calculation of the SKE budget involves along-front decomposition, for computational efficiency we first divide 100 km along  $y$  into 16 same-size chunks. A sensitivity test using 4 chunks gives visually the same mean fields. Then we compute the along-front averages for each chunk and take the overall average at the end as the final result. The resulting mean fields show reasonable smoothed profiles highlighting the frontal and Ekman flows in  $v^a$  and  $u^a$ , respectively (Fig. 7bc blue colors). A mean secondary vertical flow  $w^a$  is also obvious around the mean temperature front  $T^a$  (Fig. 7ad), likely an averaged ageostrophic response to strain and BLT (Shakespeare & Taylor 2013; Crowe & Taylor 2018). To eliminate boundary effects in filtering, we only average the 5 km range around the center for each chunk, giving 90 % along-front coverage.

### 5.2. Mesoscale stirs heterogeneous energy distribution and conversion

To obtain the evolution equation for SKE  $\equiv \frac{1}{2}\mathbf{u}^s \cdot \mathbf{u}^s$ , we start from the momentum equations governing the filtered velocity  $\bar{\mathbf{u}}$  (Verma *et al.* 2022)

$$\frac{\partial \bar{u}_i}{\partial t} + \frac{\partial \bar{u}_i}{\partial x_j} (\bar{u}_j + \bar{U}_j) + \epsilon_{i3k} f \bar{u}_k = -\bar{\varphi}_j + \alpha g \bar{T} \delta_{i3} + \bar{F}_{u_i} - \frac{\partial \tau_{ij}}{\partial x_j}, \quad (5.1)$$

where  $\tau_{ij} = \overline{u'_i u'_{total,j}} = \overline{u_i (u_j + U_j)} - \bar{u}_i (\bar{u}_j + \bar{U}_j) \approx \overline{u_i u_j} - \bar{u}_i \bar{u}_j$  is BLT residual stress. Subtracting the along-front average from (5.1) and taking the dot product with  $\mathbf{u}^s$  gives

$$\frac{\partial \text{SKE}}{\partial t} = P^a + P^s + P' + B^s + A^s, \quad (5.2)$$

where

$$P^a = -[\mathbf{u}^s(\mathbf{u}^s + \mathbf{U})] : \nabla \mathbf{u}^a, \quad (5.3a)$$

$$P^s = -\langle \mathbf{u}^s(\mathbf{u}^s + \mathbf{U}) \rangle : \nabla \mathbf{u}^s, \quad (5.3b)$$

$$P' = \left( \overline{u' u'_{total}} - \langle \overline{u' u'_{total}} \rangle \right) : \nabla \mathbf{u}^s, \quad (5.3c)$$

$$A^s = -\nabla \cdot \left\{ \bar{u}_{total} \text{SKE} + \mathbf{u}^s \varphi^s + \mathbf{u}^s \cdot \left[ \left( \overline{u' u'_{total}} - \langle \overline{u' u'_{total}} \rangle \right) - \langle \mathbf{u}^s(\mathbf{u}^s + \mathbf{U}) \rangle \right] \right\} \quad (5.3d)$$

are the along-front mean, submesoscale, and BLT productions with  $\mathbf{a}\mathbf{b} : \nabla \mathbf{u} = a_i b_j u_{i,j}$ , and advects of SKE by total velocity and of submesoscale geopotential and residual stresses by  $\mathbf{u}^s$ .  $B^s = w^s b^s$  is the submesoscale buoyancy production. Importantly, the term  $B^s$  captures the transfer of frontal PE reservoir to SKE through BI (Verma *et al.* 2022), and its average are central to ML parameterizations in large-scale models (Fox-Kemper *et al.* 2008; Bodner *et al.* 2023). The evolution equation for TKE is

$$\frac{\partial \text{TKE}}{\partial t} = P_H + P_V + B + A, \quad (5.4)$$

where the horizontal and vertical productions are (Germano 1992)

$$P_H = -\overline{u' u'_{total}} \frac{\partial \bar{u}}{\partial x} - \overline{u' v'_{total}} \frac{\partial u^s}{\partial y} - \overline{v' u'_{total}} \frac{\partial \bar{v}}{\partial x} - \overline{v' v'_{total}} \frac{\partial v^s}{\partial y}, \quad (5.5a)$$

$$P_V = -\overline{u' w'_{total}} \frac{\partial \bar{u}}{\partial z} - \overline{v' w'_{total}} \frac{\partial \bar{v}}{\partial z} - \overline{w'^2_{total}} \frac{\partial \bar{w}}{\partial z} - \overline{w' u'_{total}} \frac{\partial \bar{w}}{\partial x} - \overline{w' v'_{total}} \frac{\partial w^s}{\partial y}, \quad (5.5b)$$

$B = \overline{w' b'}$  is buoyancy production, and  $A$  is advection and dissipation, respectively. Note that the horizontal stresses in  $P_H$  and  $P_V$  have additional asymmetric though minor stress contribution directly from background mesoscale forcing  $\mathbf{U}$ , and that shear components have contributions from both along-front mean  $\mathbf{u}^a$  and submesoscale deviation  $\mathbf{u}^s$ . And by comparing the pattern of  $P'$  to those of  $P_H$  and  $P_V$ , we can examine if the along-front mean shear or the submesoscale shear are dominant, which is a preferred choice when further decompositions become computationally challenging. The analysis below demonstrates that  $P'$  and  $P_H$  represent virtually the same submesoscale-BLT transfer in opposite directions, and that  $P_V$  has significant contributions from both surface-intensified Ekman and frontal geostrophic shears. Although the direct contribution of mesoscale forcing  $\mathbf{U}$  mainly appears in the total velocity components, its significance can accumulate

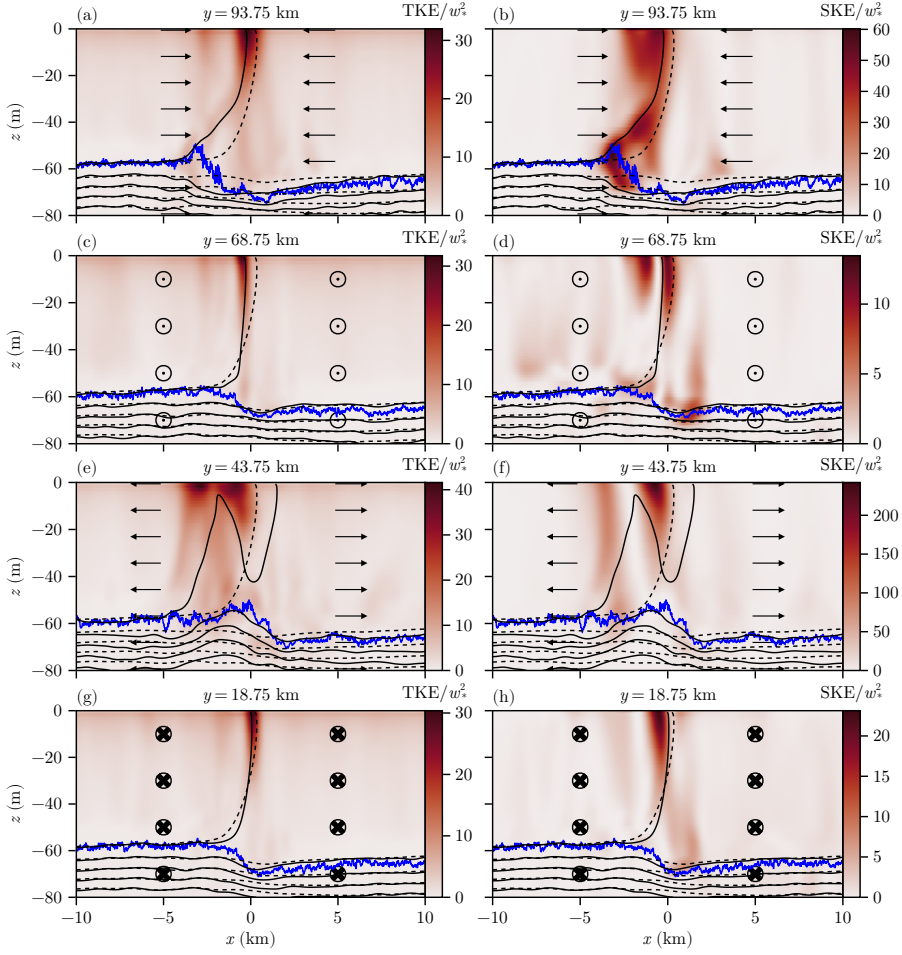


Figure 8. TKE and SKE at 30 h along  $y = 93.75, 68.75, 43.75$ , and  $18.75$  km following the mean frontal flow (Fig. 7b). Note that scales of the colorbars differ with locations and between TKE and SKE. Arrows indicate velocity vectors of the background mesoscale eddy forcing.

steadily in time and space. Here the geostrophic shear production is

$$P_{Vg} = \frac{\overline{u'w'} \partial \bar{b}}{f} - \frac{\overline{v'w'} \partial \bar{b}}{f}, \quad (5.6)$$

and we can also examine similar geostrophic components in  $P^a$  and  $P^s$  to clarify generation or destruction of SKE through the mean flow and self-interaction. Moreover, we do not include dissipation terms in (5.2) and (5.4) since the model only implements implicit numerical dissipation through the advection scheme (Silvestri *et al.* 2024).

Four vertical slices show drastically different budget contributions, especially right downstream of the strain extrema (Figs. 8–11). Specifically, we follow the mean frontal flow direction and choose  $y = 93.75, 68.75, 43.75$ , and  $18.75$  km. The strain is converging and diverging at  $y = 93.75$  and  $43.75$  km, respectively, while background eddy flow is augmenting and opposing the frontal flow respectively at  $y = 68.75$  and  $18.75$  km. The choice of slightly downstream locations from the strain extrema is supported by

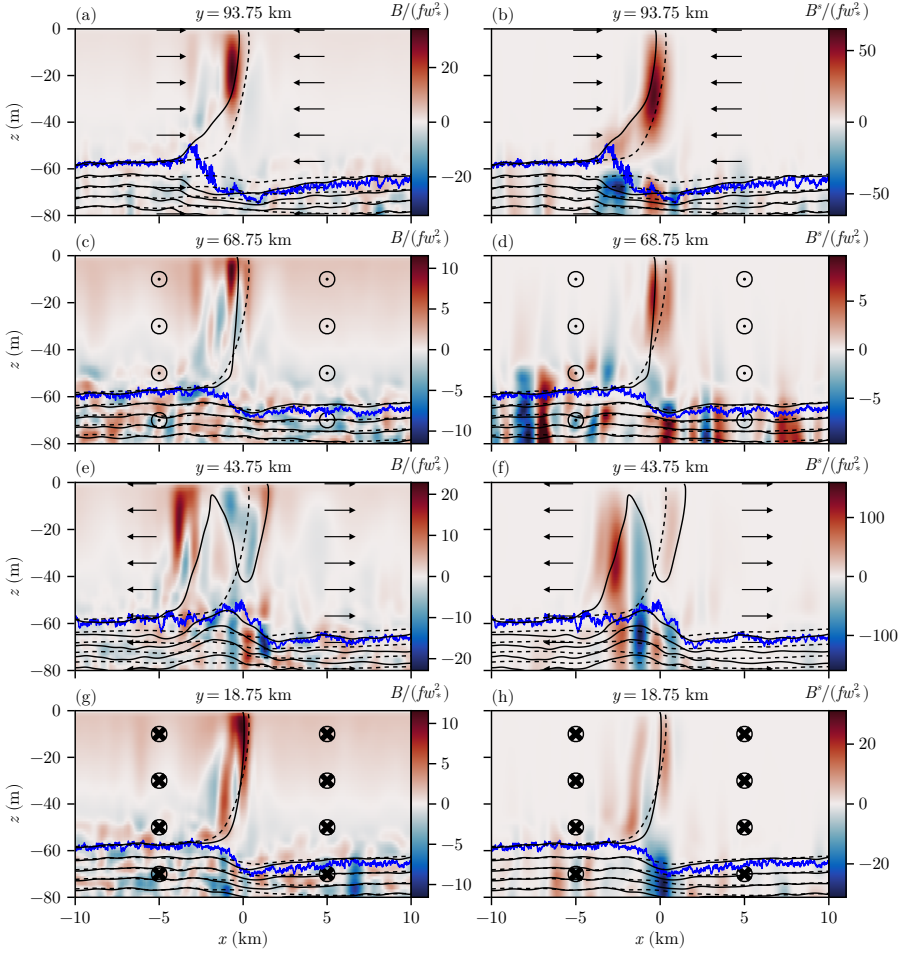


Figure 9. TKE buoyancy production  $B$  and SKE buoyancy production  $B^s$  at 30 h along  $y = 93.75, 68.75, 43.75$ , and  $18.75$  km following the mean frontal flow (Fig. 7b). Note that scales of the colorbars differ with locations and between  $B$  and  $B^s$ . Arrows indicate velocity vectors of the background mesoscale eddy forcing.

the advection of frontal flow in the negative  $y$  direction, consistent with patterns on the horizontal slices of TKE and SKE (Fig. 5cd). These slices reveal how the large-scale flow modulates the local stratification, the distribution of kinetic energy, and the dominant terms in the turbulent and submesoscale energy budgets.

The stratification at each slice deviates significantly from the along-front average, particularly in regions under extreme mesoscale strains (Figs. 8–11 solid vs. dash contours). Specifically, in the strong convergence region (e.g., at  $y = 93.75$  km), the frontal isotherm exhibits a slope close to that of the along-front mean isotherm above  $z = -30$  m, but its slope below appears flatter, indicative of submesoscale restratification near the edge of local SKE extreme (Figs. 5d). Isotherms around  $x = 0$  in the transition layer below  $z = -60$  m are displaced deeper compared with their along-front mean counterparts, suggesting mesoscale convergence-driven downwelling. In contrast, in the region under strong divergence ( $y = 43.75$  km), the frontal isotherm is dramatically distorted, showing significant curvature and heaving that implies more remarkable submesoscale stirring near the centre of local SKE extreme (Figs. 5d). Here, isotherms in the transition layer

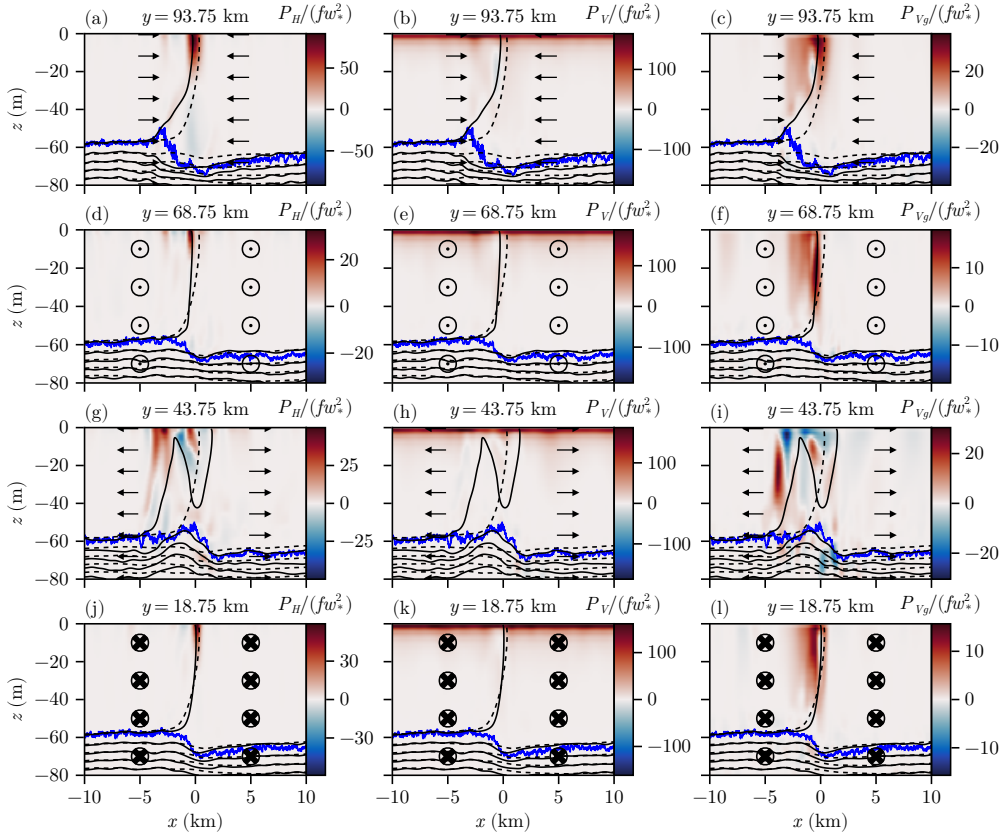


Figure 10. TKE horizontal production  $P_H$ , vertical production  $P_V$ , and geostrophic vertical production  $P_{Vg}$  at 30 h along  $y = 93.75, 68.75, 43.75$ , and  $18.75$  km following the mean frontal flow (Fig. 7b). Arrows indicate velocity vectors of the background mesoscale eddy forcing.

are shallower than those in the along-front average, consistent with divergent strain and submesoscale-induced upwelling. The other two slices ( $y = 18.75$  and  $68.75$  km), located in regions of weaker strain, show a frontal structure better resembles the along-front average, though with steeper slopes, perhaps due to locally dominant mixing that deepens the ML.

The vertical distributions of TKE and SKE reflect these differing dynamical regimes (Fig. 8). At the convergent-influenced slice ( $y = 93.75$  km), TKE is confined to the near-surface frontal isotherm, whereas SKE is about twice as large in both magnitude maximum and spatial extent, extending more to the left of the frontal isotherm and throughout the depth of the mixed layer (Fig. 8ab). This contrast consistently reveals that frontogenesis could be dominant above  $z = -30$  m where both TKE and SKE are strong, while submesoscale restratification controls the deeper frontal isotherm where only SKE is significant. Further downstream of the convergence zone ( $y = 68.75$  km), TKE is more tightly confined in  $x$  with similar magnitude, likely due to cumulative strain impact, while SKE maximum is dramatically reduced to just half of TKE maximum (Fig. 8cd). The frontal isotherm splits SKE into a bimodal pattern above  $z = -40$  m, likely due to differences between the local meandering front and its along- $y$  average. The most complex pattern appears slightly downstream of the divergent zone ( $y = 43.75$  km), where the

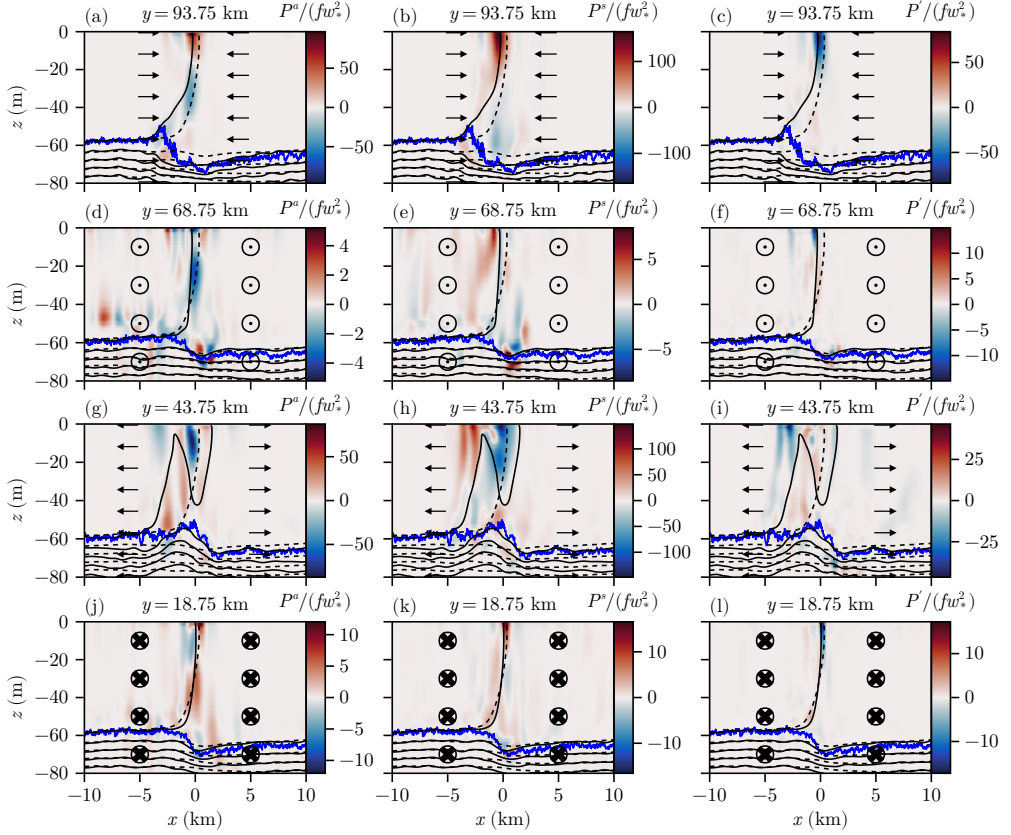


Figure 11. SKE mean-flow production  $P^a$ , submesoscale and turbulent production  $P^s$ ,  $P'$  at 30 h along  $y = 93.75, 68.75, 43.75$ , and  $18.75$  km following the mean frontal flow (Fig. 7b). Arrows indicate velocity vectors of the background mesoscale eddy forcing.

strong curvature of the isotherm organizes both TKE and SKE into a bimodal structure (Fig. 8ef). TKE remains surface-intensified, while the two SKE modes are vertically distinct and extend to the two lower turning points of the frontal isotherm. Two TKE modes have similar maximum slightly higher than other slices, but SKE is dominant by the right mode with a maximum about four times that along  $y = 93.75$  km. We confirm later that this bimodal structure roughly corresponds to opposite energy transfer between TKE and SKE based on budget analysis. In regions of weaker strain ( $y = 18.75$  km), TKE is concentrated similar to that along  $y = 68.75$  km, while SKE is comparable in strength and confined mainly to one side of the isotherm (Fig. 8gh). To clarify the evolution of these heterogeneous across-front structures, we analyze terms in energy budgets of TKE and SKE.

The vertical buoyancy flux, a key energy conversion term, is most active near the strain extrema (Fig. 9). Near the converging zone ( $y = 93.75$  km), the TKE vertical buoyancy flux  $B$  is positively concentrated around the frontal isotherm above  $z = -40$  m (Fig. 9a), indicating transfer to TKE from PE reservoir charged by surface cooling and Ekman-induced buoyancy flux (e.g., Thomas 2005; Skillingstad *et al.* 2017; Verma *et al.* 2022). The dominant mode of the SKE buoyancy flux  $B^s$  is wider, twice stronger, centered around  $z = -30$  m, and reaching to the base of the ML (Fig. 9b), representative of impact from

submesoscale BI (Fox-Kemper *et al.* 2008; Johnson & Fox-Kemper 2024). The SKE flux  $B^s$  also shows fluctuating components in the transition layer, highlighting the more complex submesoscale processes other than BI like frontal overturning. These fluxes are weaker further downstream along  $y = 68.75$  km with comparable spatial extent (Fig. 9cd). In particular,  $B^s$  appears to be an order of magnitude smaller than its upstream counterpart and comparable to the collocated  $B$  in terms of maximum.

At the divergence-influenced slice ( $y = 43.75$  km), both buoyancy fluxes show a positive-negative dipole around the up-and-down frontal isotherm (Fig. 9ef). While the dipole for  $B$  is confined near the surface and split by the tip of the curved isotherm, the  $B^s$  dipole is located along and below the isotherm, extending even below the ML base (Siegelman *et al.* 2020). The  $B^s$  maximum magnitude here is more than twice that along  $y = 93.75$  km and controls the deeper SKE pattern left of its maximum (Fig. 8f), yet the magnitude maximum of  $B$  is lower than that in the converging zone. The vertical buoyancy fluxes along  $y = 18.75$  km shows more vertical extent for  $B$  yet weak ML component for  $B^s$ . The magnitude maximum for  $B$  is comparable to that along  $y = 68.75$  km with yet wider extent, while a strong negative flux in  $B^s$  appears in the transition layer at  $x = 0$  and more than double the magnitude maximum of that along  $y = 68.75$  km. These drastically diverse patterns highlight how background mean flow, submesoscales and BLT interact closely to affect the buoyancy fluxes.

For the TKE budget specifically, the vertical buoyancy flux is less dominant than shear production terms (Fig. 10). Generally, horizontal shear production  $P_H$  is positively concentrated at the frontal isotherm, consistent with energy transfer due to frontogenesis, while vertical shear production  $P_V$  is dominated by near-surface Ekman shear except the front-concentrated geostrophic contribution. In particular, at  $y = 93.75$  km, the  $P_H$  pattern resembles that of SKE and that of BLT-to-SKE transfer  $P'$  with a sign-flip (Fig. 10a, 8a, 11a), consistent with downscale energy transfer under frontogenesis (Srinivasan *et al.* 2023). That for  $P_V$  is near-uniformly positive in the surface Ekman layer above  $z = -10$  m (Fig. 10b), while its geostrophic component  $P_{Vg}$  is dominantly positive around the frontal isotherm (Fig. 10c), indicative of possible presence of symmetric instabilities (e.g., Thomas *et al.* 2013; Skillingstad *et al.* 2017; Wenegrat 2023). At  $y = 68.75$  km,  $P_H$  has negligible horizontal extent, and  $P_V$  remains Ekman-dominated with similar front-concentrated geostrophic contribution (Fig. 10def). At  $y = 43.75$  km,  $P_H$  is positive to the negative- $x$  side of the frontal isotherm and turns into a dipole just right to the isotherm tip, while the geostrophic component of  $P_V$  shows two dipoles at both locations (Fig. 10gi). This complex pattern again demonstrate intricate coupling between BLT and submesoscale BI on the shear structure, regardless of the near-identical pattern in the full  $P_V$  (Fig. 10i). At  $y = 18.75$  km, the flux patterns resemble those along  $y = 68.75$  km (Fig. 10jkl).

The SKE budget further highlights the impact of large-scale mean flow and self-generation (Fig. 11). Near the convergence zone ( $y = 93.75$  km), the budget is dominated by the submesoscale self-production  $P^s$  near the surface, indicating local frontogenetic sharpening (Fig. 11ab). Conversely, near the divergence zone ( $y = 43.75$  km), both the production from the along-front mean flow  $P^a$  and the self-production term contribute significantly negative, creating a complex pattern of energy extraction and redistribution around the curved frontal isotherm (Fig. 11gh). Across slices away from the strain extrema, all SKE production terms are comparatively weak. Geostrophic components in both  $P^a$  and  $P^s$  are generally concentrated around mid-depth of the ML and less than half of the full productions in term of maximum (not shown), suggesting the significance of ageostrophic impact in the SKE budget. Patterns of BLT-extraction  $P'$  are virtually identical to those of  $P_H$  with a flip of sign. This detailed budget analysis implies that the inhomogeneous

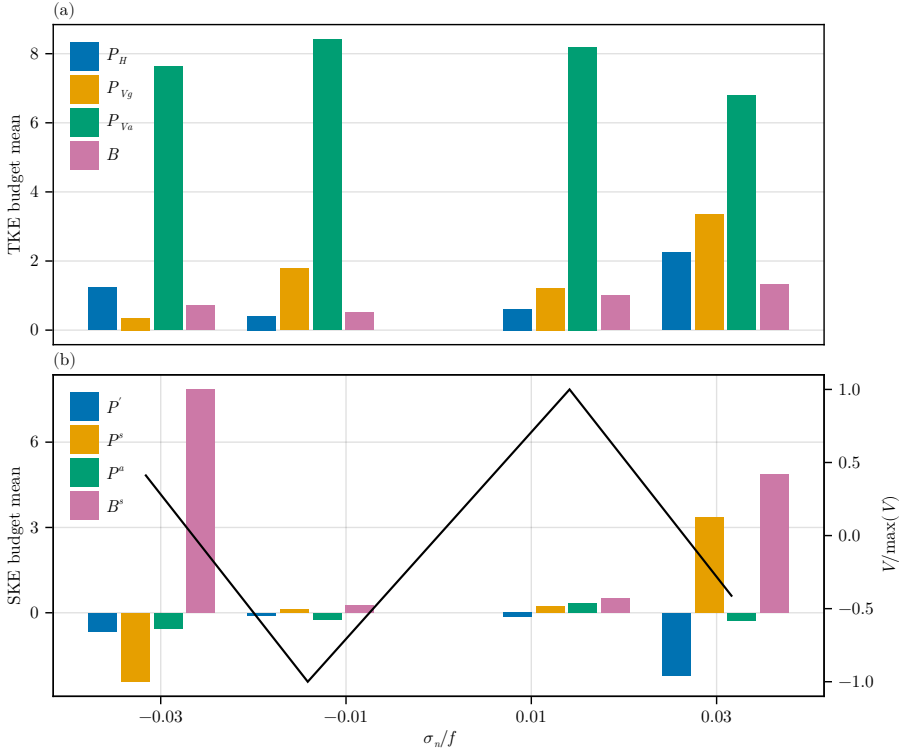


Figure 12. Aggregated barplots of mean (a) TKE productions, and (b) SKE productions at four slices with different mesoscale strain  $\sigma_n/f$ . The spatial average is computed for  $x \in [-4 \text{ km}, 4 \text{ km}]$  and above the local MLD. The black curve in (b) shows the normalized mesoscale velocity in  $y$  at the four slices.

mesoscale eddy field does not merely influence the frontal structure, but actively selects and amplifies different energy budget contributions between SKE and TKE at different locations along the front.

An aggregated barplot clarify these dramatic energy budget changes with the mesoscale background (Fig. 12). Specifically, we use a cross-front mean for  $x \in [-4 \text{ km}, 4 \text{ km}]$  and above the local MLD to aggregate various contributions along each vertical slice. For TKE, the mean production is dominated by the vertical ageostrophic shear due to BLT  $P_{Va} = P_V - P_{Vg}$ , while the geostrophic shear production can differ by about an order of magnitude between slices located in the most negative and positive strain regions, with normalized mean  $P_{Vg}$  smaller than 0.35 and greater than 3.3, respectively (Fig. 12a). The mean horizontal shear production  $P_H$  is stronger than that of  $P_{Vg}$  only with the most negative strain. The mean buoyancy flux  $B$  is generally moderate across slices, regardless of its totally different spatial pattern (Fig. 9 left column). For SKE, the aggregation illustrates a correlation between strong productions and strong strains, similar to that between strain and SKE itself (Fig. 12b). In particular, the vertical buoyancy flux  $B^s$  dominate the production for all slices and is the largest and only production term in the diverging strain region. The submesoscale self-production  $P^s$  is the strongest destruction term here but the second largest production in the converging strain region. The BLT-destruction  $P'$  contributes to  $P_H$  and has a similar pattern as that for  $P_H$  with a negative sign as expected. The average-flow production  $P^a$  is mild and negative at three out of four slices. All terms are weak on slices with moderate normal strains yet strongest meridional advection  $V = \pm \max(V)$ .

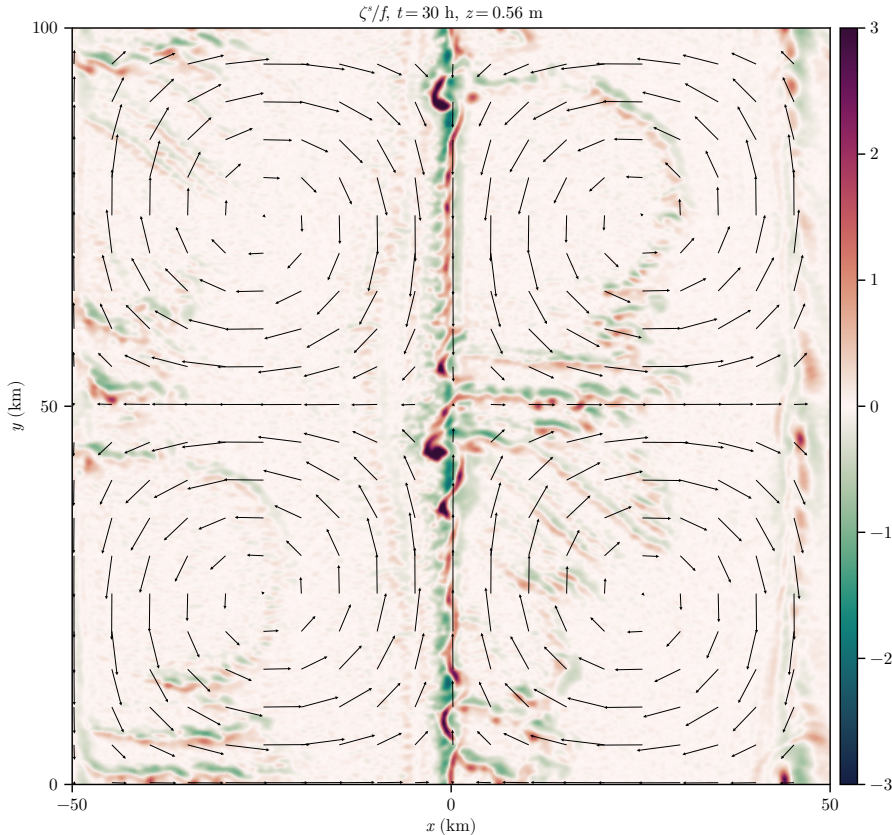


Figure 13. Normalized submesoscale vertical vorticity  $\zeta^s/f$  at  $t = 30$  h,  $z = -0.56$  m. Note that the along-front component in Fig. 3 is absent due to flow decomposition. Arrows indicate velocity vectors of the eddy forcing.

An alternative aggregation using productions at the TKE or SKE maxima shows a distinct pattern and much stronger across-slice variations and on-slice values, confirming the local spatial heterogeneity across the front (Fig. 16).

### 5.3. Secondary mesoscale–Ekman effects

The asymmetric development of the vorticity bands is a unique feature in the simulation (Fig 3bcd). This asymmetry appears also in the divergence plot and could result dynamically from the mesoscale eddy field and surface wind as a secondary effect (Fig 2bc). In particular, the long, nearly zonal streaks of vorticity observed in the divergence regions around  $y = 50$  km resemble edge-wave activity on sharp potential-vorticity (PV) gradients, often described in the PV-staircase framework (e.g., Dritschel & McIntyre 2008; Dunkerton & Scott 2008; Scott & Dritschel 2012; Khatri & Berloff 2018). On the other hand, the other band group in the convergence region aligns with the background eddy velocity vectors. This is qualitatively consistent with VRWs trapped on the radial PV gradient of mesoscale eddies (McWilliams *et al.* 2003). For instance, the prescribed cyclonic eddies have a maximum vertical vorticity at the center and a mostly negative radial vorticity gradient (Fig 2b). Under the theory of VRWs, a similar PV gradient background can hold instability modes around the vortex, similar to perturbation patterns in the full-domain submesoscale vorticity field (Fig. 13).

To explore this analytically, we consider a linear, non-hydrostatic, unstratified system away from the front:

$$\left[ \frac{\partial}{\partial t} + (\mathbf{U}^a + \mathbf{U}) \cdot \nabla \right] \mathbf{u}^s + f \hat{z} \times \mathbf{u}^s = -\nabla \varphi^s + b^s \hat{z}, \quad (5.7a)$$

$$\left[ \frac{\partial}{\partial t} + (\mathbf{U}^a + \mathbf{U}) \cdot \nabla \right] b^s = 0, \quad (5.7b)$$

$$\nabla \cdot \mathbf{u}^s = 0, \quad (5.7c)$$

where  $\mathbf{U}^a = (U^a, V^a)$  is a horizontally uniform Ekman flow, representing the leading order component of  $\mathbf{u}^a$  away from the front. Assuming a plane wave solution  $\propto \exp[i(k_1 x + k_2 y + k_3 z - \omega t)]$ , the system of equations can be written as

$$\begin{pmatrix} a & -f & 0 & 0 & -k_1 \\ f & a & 0 & 0 & -k_2 \\ 0 & 0 & a & 0 & -k_3 \\ 0 & 0 & 0 & a & 0 \\ k_1 & k_2 & k_3 & 0 & 0 \end{pmatrix} \begin{pmatrix} \hat{u}^s \\ \hat{v}^s \\ \hat{w}^s \\ \hat{b}^s \\ \hat{\varphi}^s \end{pmatrix} = 0, \quad (5.8)$$

where  $a = \omega - (\mathbf{U}^a + \mathbf{U})k_1 - (V^a + V)k_2 = \omega - (\mathbf{U}^a + \mathbf{U}) \cdot \mathbf{k}_h$  is the intrinsic frequency Doppler-shifted by the large-scale Ekman and mesoscale flows, with  $\mathbf{k}_h = (k_1, k_2)$ . For a non-trivial solution, the determinant of the coefficient matrix must be zero. This yields two branches of solutions: the passive tracer advection mode ( $a = 0$ ) from the fourth row, and the wave modes from the remaining system. The corresponding dispersion relation is

$$\omega(k_1, k_2, k_3) = (\mathbf{U}^a + \mathbf{U}) \cdot \mathbf{k}_h \pm f \frac{k_3}{\sqrt{k_1^2 + k_2^2 + k_3^2}}. \quad (5.9)$$

This relation, which describes advected inertial waves, demonstrates that the wave frequency is directly modulated by the mesoscale and Ekman velocities. Thus, relevant wave modes can be locally induced and modified by the background flow. We note that this idealized derivation is not equivalent to a full wave-mean-flow interaction or a classical PV analysis, as it ignores stratification and the advection of the background mesoscale field. However, it serves to demonstrate that the simulated secondary effects are qualitatively consistent with known wave-mean-flow dynamics.

Moreover, the simulated asymmetry is likely a product of both the Ekman drift and the intrinsic cyclonic-anticyclonic instability asymmetry. The vorticity groups are adjacent to the right (positive  $x$ ) yet absent to the left of the unstable front, likely due to Doppler selection by the background flow, including the westward surface Ekman drift. Furthermore, anticyclonic vortices are known to be more susceptible to ageostrophic instabilities, which could prevent the formation of a comparable coherent pattern to that seen in the cyclonic regions (e.g., Yim *et al.* 2019; Kafiabad *et al.* 2021). And the two main SKE growing modes could further arise from submesoscale front-wave interactions (e.g., Hilditch *et al.* 2025). Therefore, while conventional wave theories provide a basis for interpretation, the specific location and character of frontal instabilities induced by this coupling will vary with the setup of the front, eddies, and wind.

Nevertheless, this evolution highlights a secondary pathway for mesoscale influence, where the background field modulates submesoscale BI and coupled BLT along the front during the early stages of evolution. This interaction can only be resolved in a nonhydrostatic setup with both a large enough domain size and fine enough resolution, and we find that the discussed vorticity pattern is absent in a lower resolution hydrostatic run with parameterized

boundary layer physics (Fig. 17). The hydrostatic run shares the same configuration with the LES present here except a coarse horizontal spacing  $\Delta h = 156.25$  m, a hydrostatic solver, and a BLT parameterization (Wagner *et al.* 2024). Since the secondary effect is also absent in a non-hydrostatic run with the same horizontal spacing  $\Delta h = 156.25$  m that underresolves BLT (not shown), the resolution would also be critical. Although the pattern of this effect is uniquely maintained in the large simulation and triggers early ML instabilities, later evolution tends to be dominated by the cumulative impact of mesoscale strain as described in the previous section (Fig. 3bc vs. d). Finally, we note that while the along-front profiles in §5.1 suggest significant correlations between SKE and the mesoscale strain  $\sigma_n$ , this analysis offers an alternative mechanism.

## 6. Discussion and conclusions

This study presents, to our knowledge, the first Large Eddy Simulation (LES) framework to resolve submesoscale and boundary layer turbulence (BLT) within a persistent, spatially heterogeneous mesoscale field. The primary finding is that mesoscale heterogeneity induces a first-order control on the evolution, structure, and energetics of an unstable front and its associated turbulence. By moving beyond the classical uniform-strain paradigm, we demonstrate that the background mesoscale field actively organizes submesoscale and BLT interactions, creating a spatial pattern of turbulent hotspots whose locations are tied to the underlying large-scale flow.

Our model setup integrates a prescribed mesoscale forcing with a two-sided mixed layer front initially in geostrophic balance (Thomas & Ferrari 2008; Hamlington *et al.* 2014). Thanks to the computational power of distributed GPUs and the Oceananigans configuration (Ramadhan *et al.* 2020), our model is able to resolve BLT under the mesoscale forcing. The excitation of BLT by surface wind stress and cooling is fast, and the front with along-front wind component experiences destabilizing Ekman buoyancy flux that advects cold over warm waters (e.g., Thomas 2005; Wenegrat 2023), developing significant along-front variabilities of front width, curvature, mixed-layer depth (MLD), and other frontal properties under mesoscale forcing. These variations correlate strongly with the background mesoscale, in particular for which convergence (divergence) reduces(increases) the frontal width yet deepens(shoals) the MLD.

A triple flow decomposition allowed us to quantify the kinetic energy budgets for BLT (TKE) and submesoscales (SKE) and examine their spatial variability across distinct dynamical regimes. We observed that extreme mesoscale strain collocates with both amplified production and destruction terms, and strong divergence further coupled to significant cross-sectional variability. Specifically, under strong mesoscale convergence, TKE production via horizontal and vertical geostrophic shear is maximized. Here, the mean geostrophic shear production reaches approximately half the magnitude of the ageostrophic term, a ratio consistent with the presence of a strong submesoscale source, though ageostrophic production remains dominant (Dong *et al.* 2024). Similarly, SKE self-production and destruction by BLT are enhanced in convergent zones. Conversely, under strong divergence, the self-production term becomes negative, acting as a sink, while the vertical buoyancy flux remains as the dominant source for SKE, highlighting its critical role in sustaining submesoscale instabilities such as baroclinic instability.

These findings offer critical context for interpreting previous process studies. While prior high-resolution LES utilizing zero or uniform background strain have focused on budget analysis under volume-wise or along-front averaging (Sullivan & McWilliams 2018; Verma *et al.* 2022; Bodner *et al.* 2023; Johnson & Fox-Kemper 2024), our results clarify that the multiscale energy budget contributions can be spatially intermittent under

heterogeneous mesoscale forcing. The simultaneous coexistence of these opposing yet connected dynamical regimes requires more careful budget formulations than those in strain-free or uniform-forcing models. Furthermore, compared to hydrostatic regional models which capture mesoscale to submesoscale variability but parameterize BLT (e.g., Srinivasan *et al.* 2023), our explicit resolution of non-hydrostatic BLT reveals order-of-magnitude along-front variability in TKE fluxes with distinct spatial patterns under larger-scale modulation. This suggests that hydrostatic models may systematically underestimate certain variabilities of vertical mixing in frontal regions due to lack of enough large-scale coupling in current subgrid-scale parameterizations.

These results also have significant implications for the representation of upper ocean dynamics in large-scale models. The pronounced along-front heterogeneity in TKE and SKE implies that vertical transport of heat, carbon, and other tracers is likewise highly localized (Sinha *et al.* 2023; Mahadevan 2016; Taylor & Thompson 2023; Ferrari 2011; Su *et al.* 2018). Our budget analysis confirms that domain-integrated vertical fluxes are likely dominated by these distinct hotspots. Moreover, the results suggest that the mesoscale field, along with surface forcing, could selectively trigger submesoscale instabilities via secondary perturbations, rather than allowing broad, random growth along the front. This indicates a dynamic coupling between mesoscale-driven and instability-driven submesoscale processes that have conventionally been treated in isolation. The drastic variability in budget fluxes implies that current climate and general circulation models likely miss crucial, spatially intermittent interactions (Bachman *et al.* 2017; Bodner *et al.* 2023). These insights were only possible due to the unique combination of a 100 km-domain, which holds the mesoscale, and meter-scale grid resolution, which resolves the non-hydrostatic dynamics.

We acknowledge certain idealizations necessary to isolate the target physics. The upper limit on resolved scales is set by the 100 km domain, and the imposed mesoscale forcing follows a controlled quadrupole pattern without an eddy-driven surface temperature signature. The absence of feedback terms to the mesoscale flow in the momentum equations also breaks the clarity in formulating derivative budgets like those for vorticity, since the derivation will involve isolated horizontal gradients of  $\mathbf{U}$ . In the vertical, the 250 m depth and the absence of a full thermocline constrain interactions with the deep ocean. Finally, the integration time captures the transient adjustment of the front rather than a full mesoscale-submesoscale equilibrium. In future studies we will report on the extended integration time of the simulation when turbulence is fully developed. These choices, however, are what define this as a controlled numerical experiment, allowing us to isolate the specific mechanism of mesoscale-submesoscale-BLT coupling from the full complexity of a realistic ocean energy cascade. The sensitivity of quantitative correlations to model setup and initialization remains an important area for investigation (Atkinson *et al.* 2025).

The versatility of this framework extends its utility beyond the current study. The explicit resolution of fine-scale frontal features provides a rich dataset for testing and refining subgrid-scale parameterizations for coarser-resolution ocean models. Our findings strongly suggest that such parameterizations must be scale-aware and, crucially, location-aware accounting for the local mesoscale strain and vorticity (Perezhogin *et al.* 2024; Bodner *et al.* 2025). The model can also be adapted to investigate multiscale influences on tracer transport, such as the vertical exchange of heat and carbon, which are vital for climate and biogeochemical studies. These applications, accelerated by GPU computation, highlight the potential of this modeling approach to guide future research and bridge the gap between small-scale turbulence and large-scale ocean circulation.

In summary, this study presents an idealized yet powerful numerical framework for investigating heterogeneous frontal turbulence in the upper ocean mixed layer. We utilized

a GPU-based LES to simulate the evolution of submesoscale and boundary layer turbulence under prescribed mesoscale field, surface wind forcing, and cooling, achieving a horizontal resolution of 4.88 m in a domain of 100 km. Compared to previous works focused on either submesoscale–BLT interactions or mesoscale–submesoscale energy transfers, our non-hydrostatic LES bridge these scales within a single simulation. Our results demonstrate that mesoscale inhomogeneity connects strongly to distinct structure and energetics of frontal turbulence. Future work can explore more realistic mesoscale representation, e.g. time-varying background velocity  $U$ , or inclusion of surface waves.

## Acknowledgements

We are thankful to Raffaele Ferrari and Gregory LeClaire Wagner for insightful initial discussions of the model development. This research used resources of the National Energy Research Scientific Computing Center, a DOE Office of Science User Facility supported by the Office of Science of the U.S. Department of Energy under Contract No. DE-AC02-05CH11231 using NERSC award BER-ERCAP0033352.

## Declaration of interests

The authors report no conflict of interest.

## Data availability statement

The code that supports the findings of this study is openly available in <https://github.com/bodner-research-group/LESSStudySetup.jl>, and the simulation data will also be openly available once properly processed. In accordance with the journal's policy, the authors declare the use of generative AI tools, specifically ChatGPT and Gemini, to assist with code debugging and the linguistic refinement of the text originally drafted by the authors. The authors have reviewed all AI-generated output and assume full responsibility for the accuracy and integrity of the final manuscript.

## Appendix A. Imposed mesoscale eddy velocity parameterization

We set the eddy velocity as a sum of four components defined in transformed coordinates centered at eddy centers. In particular, two warm-eddy centers are located at (25 km, 25 km) and (75 km, 75 km), while two cold-eddy centers are located at (25 km, 75 km) and (75 km, 25 km). The eddy radius is  $R = L_x/4 = 25$  km. For each eddy-centered polar coordinates with distance  $r$ :

$$\xi(r) = 2 \frac{R - r}{\pi R L_e} - \pi \frac{L_e - 1}{2}, \quad (\text{A } 1)$$

where  $L_e = 0.9$  is a dimensionless eddy frontal width parameter. Then we define for a warm-core eddy a few variables dependent on  $r$  and  $\xi$  as:

$$u^B = \frac{2\Phi gr}{fR^2\sigma^2} \exp\left(-\frac{r}{R^2\sigma^2}\right), \quad (\text{A } 2)$$

$$\frac{\partial b}{\partial \xi} = -\text{Int}(0 < \xi < \pi_0) gaa \Delta T^e \Delta m \frac{\sin(\xi)^2 - \cos(\xi)^2 + 1}{\pi}, \quad (\text{A } 3)$$

$$h_m = \text{Int}(\xi > \pi_0) + \text{Int}(0 < \xi < \pi_0) \left[ 1 - \frac{\pi - \xi - \sin(\pi - \xi) \cos(\pi - \xi)}{\pi} \right], \quad (\text{A } 4)$$

where  $\Phi = 0.01$  m is the barotropic vortex surface amplitude,  $\sigma^2 = 1$  is the dimensionless vortex spread,  $\pi_0 = 3.1415926535897$ , and  $\Delta T^e = 0.1$  °C is the eddy temperature difference. Then the warm-eddy tangential

velocity at polar angle  $\varphi$  is:

$$u^t(\varphi) = \begin{cases} \frac{\partial \xi}{\partial r} \frac{\partial b}{\partial \xi} \frac{2}{3f} + u^B, & \text{if } z > -h = -(m_0 + h_m \Delta m) \\ \frac{\partial \xi}{\partial r} \frac{\partial b}{\partial \xi} \frac{2(L_z+z)^3}{3f(L_z-h)^3} + u^B, & \text{otherwise} \end{cases} \quad (\text{A } 5)$$

where  $\partial \xi / \partial r = -2\pi / (RL_f)$ ,  $m_0 = 60$  m is the initial mixed-layer depth, and  $\Delta m = 30$  m is the mixed-layer depth difference scaled by  $h_m$  between warm and cold eddies. Note that the first term is a baroclinic adjustment that decrease to zero at the bottom of the domain. The velocity components in the original coordinate are  $u^t \sin(\varphi)$  and  $-u^t \cos(\varphi)$ . The velocities for cold-core eddies are similarly defined, with a different sign for  $u^B$  and  $\partial b / \partial \xi$  and  $h = m_0 - h_m \Delta m$ . The sum of all four eddy velocity fields establishes a geostrophically balanced background flow  $\mathbf{U}$ . The simulations use  $\mathbf{U}$  only to advect horizontal velocities and temperature, and we assume that other advection terms related to  $\mathbf{U}$  are negligible on the timescales and depth relevant to this setup.

## Appendix B. Imposed initial temperature and velocity

We construct this setup by joining two profiles given by

$$\frac{M_0^2 L_f L_x}{180 \alpha g} \left[ 1 - \tanh \left( \frac{x}{L_f L_x / 90} \right) + \tanh \left( \frac{x - L_x / 2}{L_f L_x / 90} \right) \right] \left[ \tanh \left( \frac{z + m_0}{\Delta m^f} \right) + 1 \right] + \Gamma_T \quad (\text{B } 1)$$

for  $x \leq L_x / 2$ , and

$$\frac{M_0^2 L_f L_x}{180 \alpha g} \left[ \tanh \left( \frac{x - L_x / 2}{L_f L_x / 90} \right) - \tanh \left( \frac{x - L_x}{L_f L_x / 90} \right) - 1 \right] \left[ \tanh \left( \frac{z + m_0}{\Delta m^f} \right) + 1 \right] + \Gamma_T \quad (\text{B } 2)$$

for  $x > L_x / 2$ , where  $L_f = 0.9$  a dimensionless frontal width scale,  $L_x = 100$  km the zonal domain size, and

$$\Gamma_T = \frac{0.5}{\alpha g} \left\{ \left( N_s^2 + 0.1 N_T^2 \right) z + \Delta m^f \left[ \left( N_s^2 - N_T^2 \right) \ln \left( \frac{\cosh \left( \frac{z+m_0}{\Delta m^f} \right)}{\cosh \left( \frac{m_0}{\Delta m^f} \right)} \right) + 0.9 N_T^2 \ln \left( \frac{\cosh \left( \frac{z+1.5m_0}{\Delta m^f} \right)}{\cosh \left( \frac{1.5m_0}{\Delta m^f} \right)} \right) \right] \right\} \quad (\text{B } 3)$$

## Appendix C. Illustration of parameter choice

## Appendix D. Evolution of divergence

## Appendix E. Aggregated energy budgets at maximum TKE/SKE

## Appendix F. Full-domain vorticity in a hydrostatic rum

The hydrostatic simulation uses Oceananigans under the hydrostatic approximation Silvestri *et al.* (2025). The hydrostatic equations for momentum, mass conservation, sea-surface height elevation, and temperature evolution solved by the simulation are:

$$\partial_t \mathbf{u}_h = -(\mathbf{U} + \mathbf{u}_h) \cdot \nabla_2 \mathbf{u}_h - f \hat{z} \times \mathbf{u}_h - \nabla_2 p - w \partial_z \mathbf{u}_h - \partial_z \boldsymbol{\tau} - g \nabla_2 \eta, \quad (\text{F } 1)$$

$$\partial_z p = b = \alpha g T, \quad (\text{F } 2)$$

$$0 = \nabla_2 \cdot \mathbf{u}_h + \partial_z w, \quad (\text{F } 3)$$

$$\partial_t \eta = w|_{z=0}, \quad (\text{F } 4)$$

$$\partial_t T = -(\mathbf{U} + \mathbf{u}_h) \cdot \nabla_2 T - w \partial_z T - \partial_z J^T \quad (\text{F } 5)$$

where  $\mathbf{u}_h \equiv u \hat{x} + v \hat{y}$  is the horizontal velocity vector,  $\mathbf{U} \equiv U \hat{x} + V \hat{y}$  is the (divergence-free) background eddy velocity vector,  $\nabla_2 = \hat{x} \partial_x + \hat{y} \partial_y$  is the horizontal gradient. The vertical momentum stress  $\boldsymbol{\tau}$  is the wind stress  $\boldsymbol{\tau}_w$  at the surface and the vertical mixing by subgrid turbulence  $-\nu_e \partial_z \mathbf{u}_h$  in the interior. The vertical temperature flux  $J^T$  is a constant cooling  $Q$  at the surface and the vertical mixing by subgrid turbulence  $-\kappa_e \partial_z T$  in the interior. The specific BLT parameterization used here is CATKE (Wagner *et al.* 2024), and the horizontal spacing is  $\Delta h = 156.25$  m.

## Turbulent ocean front under strain

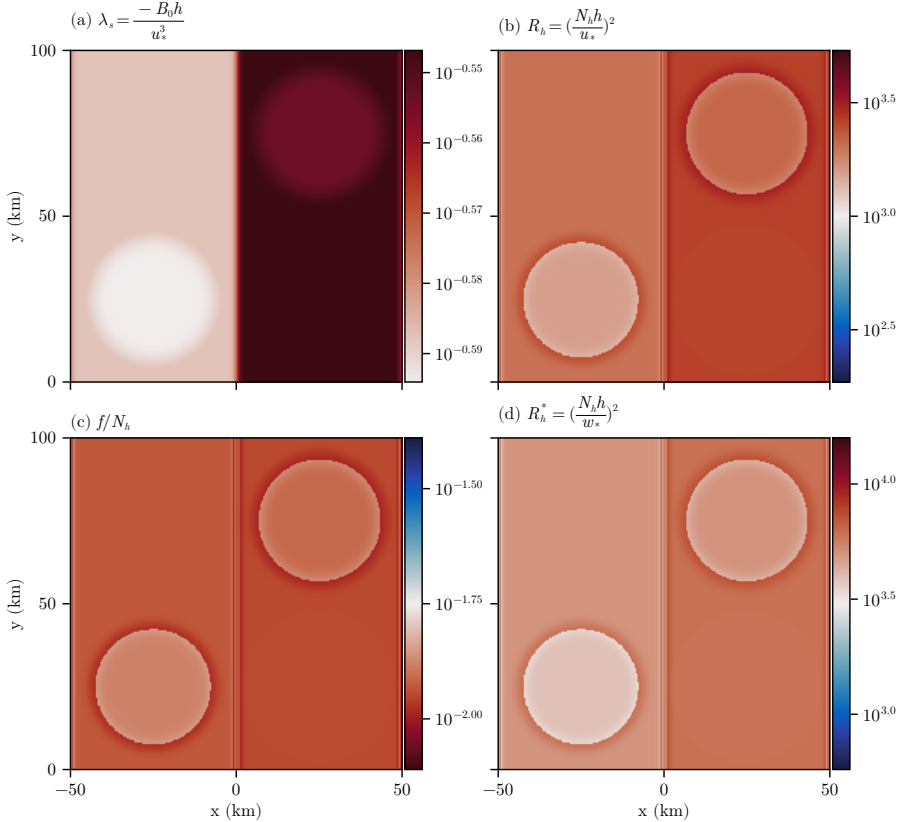


Figure 14. Initial parameter distributions for evolution of the mixed-layer depth following the framework of Legay *et al.* (2024). Shown are (a)  $\lambda_s = -B_0 h/u_*^3$  the relative contribution of the cooling and the wind, (b)  $R_h = (N_h h/u_*)^2$  and  $R_h^* = (N_h h/w_*)^2$  the stability of the mixed layer relative to the wind, (c) the importance of the Earth's rotation relative to the stratification, and (d)  $R_h^* = (N_h h/w_*)^2$  the stability of the mixed layer relative to the cooling.

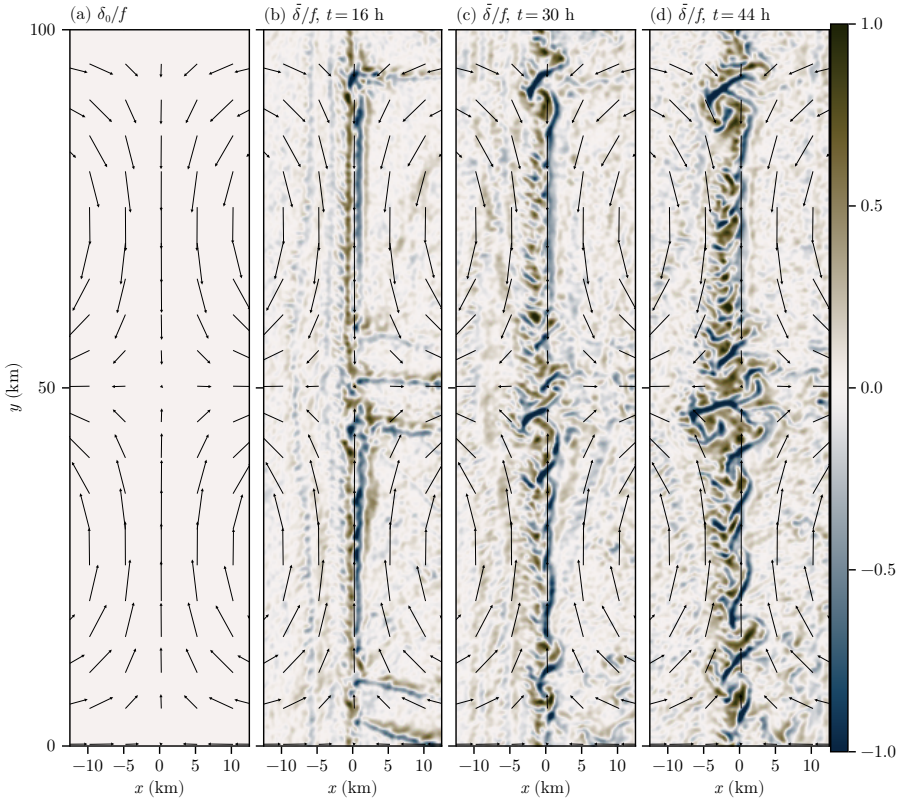


Figure 15. Snapshots of normalized surface divergence at (a) initialization, (b) 16 h, (c) 30 h, and (d) 44 h. The initial divergence in (a) is zero, while those in other panels are calculated on the meter-scale grid after a 300 m-Gaussian kernel smoothing. Arrows indicate velocity vectors of the eddy forcing.

## Turbulent ocean front under strain

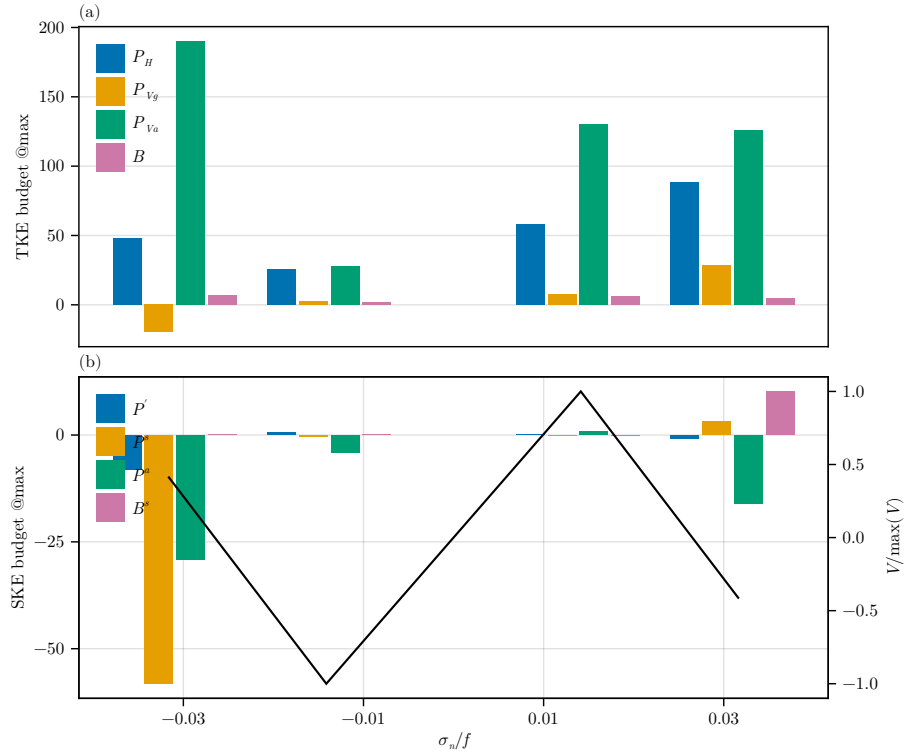


Figure 16. Aggregated barplots of (a) TKE productions, and (b) SKE productions at maximum TKE/SKE indexes across four slices with different mesoscale strain  $\sigma_n/f$ . The black curve in (b) shows the normalized mesoscale velocity in  $y$  at the four slices.

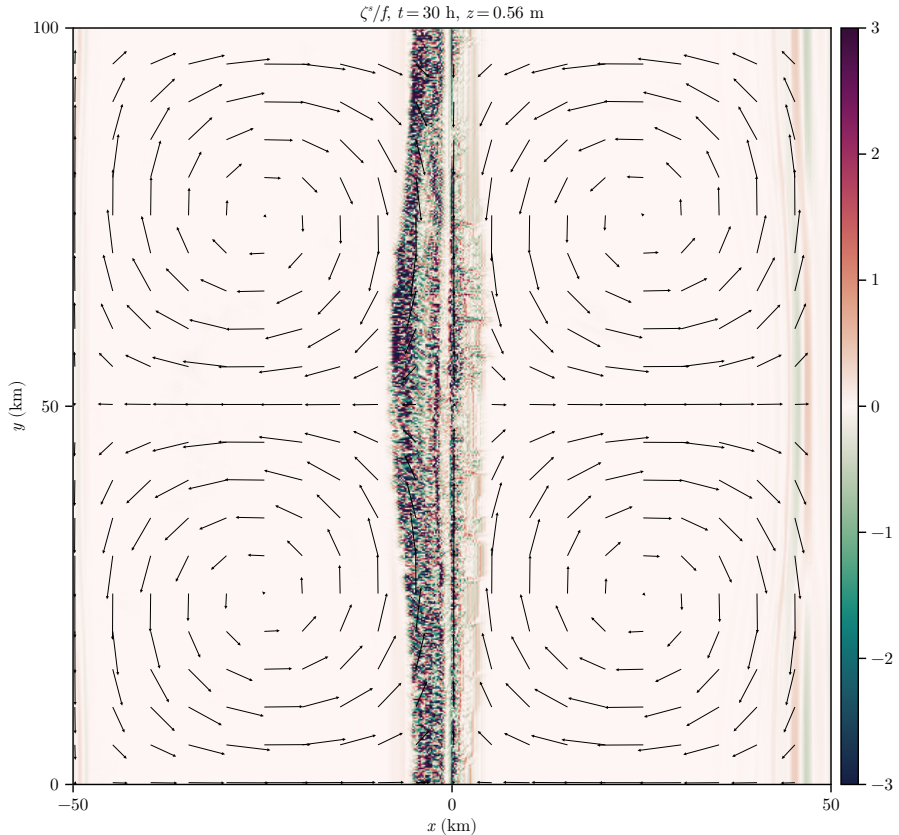


Figure 17. Normalized vertical vorticity  $\zeta^s/f$  at  $t = 30$  h,  $z = -0.56$  m. Here the coarse-graining is not necessary due to the resolution. We thus assume the raw velocities are submesoscale after subtracting an along- $y$  mean. Arrows indicate velocity vectors of the eddy forcing.

## Turbulent ocean front under strain

### REFERENCES

ATKINSON, ERIN, McWILLIAMS, JAMES CYRUS & GRISOUD, NICOLAS 2025 Near-inertial echoes of ageostrophic instability in submesoscale filaments. *Journal of Fluid Mechanics* **1015**, A17.

BACHMAN, S.D., FOX-KEMPER, B., TAYLOR, J.R. & THOMAS, L.N. 2017 Parameterization of frontal symmetric instabilities. i: Theory for resolved fronts. *Ocean Modelling* **109**, 72–95.

BODNER, ABIGAIL, BALWADA, DHRUV & ZANNA, LAURE 2025 A data-driven approach for parameterizing ocean submesoscale buoyancy fluxes. *Journal of Advances in Modeling Earth Systems* **17** (11), e2025MS004991, e2025MS004991 2025MS004991, arXiv: <https://agupubs.onlinelibrary.wiley.com/doi/pdf/10.1029/2025MS004991>.

BODNER, ABIGAIL S. & FOX-KEMPER, BAYLOR 2020 A Breakdown in Potential Vorticity Estimation Delineates the Submesoscale-to-Turbulence Boundary in Large Eddy Simulations. *Journal of Advances in Modeling Earth Systems* **12** (10), e2020MS002049, eprint: <https://onlinelibrary.wiley.com/doi/pdf/10.1029/2020MS002049>.

BODNER, ABIGAIL S., FOX-KEMPER, BAYLOR, JOHNSON, LEAH, ROEKEL, LUKE P. VAN, McWILLIAMS, JAMES C., SULLIVAN, PETER P., HALL, PAUL S. & DONG, JIHAI 2023 Modifying the mixed layer eddy parameterization to include frontogenesis arrest by boundary layer turbulence. *Journal of Physical Oceanography* **53** (1), 323 – 339.

BOYD, PHILIP W., CLAUSTRE, HERVÉ, LEVY, MARINA, SIEGEL, DAVID A. & WEBER, THOMAS 2019 Multi-faceted particle pumps drive carbon sequestration in the ocean. *Nature* **568** (7752), 327–335.

CALLIES, JÖRN & FERRARI, RAFFAELE 2018 Baroclinic instability in the presence of convection. *Journal of Physical Oceanography* **48** (1), 45 – 60.

CAPET, X., McWILLIAMS, J. C., MOLEMAKER, M. J. & SHCHEPETKIN, A. F. 2008 Mesoscale to submesoscale transition in the California current system. part ii: Frontal processes. *Journal of Physical Oceanography* **38** (1), 44 – 64.

CROWE, MATTHEW N. & TAYLOR, JOHN R. 2018 The evolution of a front in turbulent thermal wind balance. part 1. theory. *Journal of Fluid Mechanics* **850**, 179–211.

DELPECH, AUDREY, BARKAN, ROY, SRINIVASAN, KAUSHIK, McWILLIAMS, JAMES C., ARBIC, BRIAN K., SIYANBOLA, OLADEJI Q. & BUIJSMAN, MAARTEN C. 2024 Eddy–internal wave interactions and their contribution to cross-scale energy fluxes: A case study in the California current. *Journal of Physical Oceanography* **54** (3), 741 – 754.

DONG, JIHAI, FOX-KEMPER, BAYLOR, WENEGRAT, JACOB O., BODNER, ABIGAIL S., YU, XIAOLONG, BELCHER, STEPHEN & DONG, CHANGMING 2024 Submesoscales are a significant turbulence source in global ocean surface boundary layer. *Nature Communications* **15** (1), 9566.

DRITSCHEL, D. G. & MCINTYRE, M. E. 2008 Multiple jets as PV staircases: The Phillips effect and the resilience of eddy-transport barriers. *Journal of the Atmospheric Sciences* **65** (3), 855 – 874.

DUNKERTON, TIMOTHY J. & SCOTT, RICHARD K. 2008 A barotropic model of the angular momentum–conserving potential vorticity staircase in spherical geometry. *Journal of the Atmospheric Sciences* **65** (4), 1105 – 1136.

EPKE, MORITZ, LINARAKIS, LEONIDAS, KORN, PETER & BRÜGGEMANN, NILS 2025 Overturning of mixed layer eddies in a submesoscale resolving simulation of the North Atlantic. *Journal of Physical Oceanography* .

FERRARI, RAFFAELE 2011 A frontal challenge for climate models. *Science* **332** (6027), 316–317, arXiv: <https://www.science.org/doi/pdf/10.1126/science.1203632>.

FERRARI, RAFFAELE & WUNSCH, CARL 2009 Ocean circulation kinetic energy: Reservoirs, sources, and sinks. *Annual Review of Fluid Mechanics* **41** (Volume 41, 2009), 253–282.

FOX-KEMPER, B., FERRARI, R. & HALLBERG, R. 2008 Parameterization of mixed layer eddies. part i: Theory and diagnosis. *J. Phys. Oceanogr.* **38**, 1145–1165.

GERMANO, M. 1992 Turbulence: the filtering approach. *Journal of Fluid Mechanics* **238**, 325–336.

GRIFFIES, STEPHEN M., DANABASOGLU, GÖKHAN, DURACK, PAUL J., ADCROFT, ALISTAIR J., BALAJI, V., BÖNING, CLAUS W., CHASSINET, ERIC P., CURCHITSER, ENRIQUE, DESHAYES, JULIE, DRANGE, HELGE, FOX-KEMPER, BAYLOR, GLECKLER, PETER J., GREGORY, JONATHAN M., HAAK, HELMUTH, HALLBERG, ROBERT W., HEIMBACH, PATRICK, HEWITT, HELENE T., HOLLAND, DAVID M., ILYINA, TATIANA, JUNGCLAUS, JOHANN H., KOMURO, YOSHIKI, KRASTING, JOHN P., LARGE, WILLIAM G., MARSLAND, SIMON J., MASINA, SIMONA, McDougall, Trevor J., Nurser, A. J. GEORGE, ORR, JAMES C., PIRANI, ANNA, QIAO, FANGLI, STOUFFER, RONALD J., TAYLOR, KARL E., TREGUIER, ANNE MARIE, TSUJINO, HIROYUKI, UOTILA, PETTERI, VALDIVIESO, MARIA, WANG, QIANG, WINTON, MICHAEL & YEAGER, STEPHEN G. 2016 OMIP contribution to CMIP6: experimental and diagnostic protocol for the physical component of the Ocean Model Intercomparison Project. *Geoscientific Model Development* **9** (9), 3231–3296.

GULA, JONATHAN, MOLEMAKER, M. JEROEN & McWILLIAMS, JAMES C. 2014 Submesoscale cold filaments in the Gulf Stream. *Journal of Physical Oceanography* **44** (10), 2617 – 2643.

HAMINGTON, P. E., ROEKEL, L. P. VAN, FOX-KEMPER, B., JULIEN, K. & CHINI, G. P. 2014 Langmuir–

submesoscale interactions: Descriptive analysis of multiscale frontal spindown simulations. *J. Phys. Oceanogr.* **44**, 2249–2272.

HILDITCH, JAMES P., TAYLOR, JOHN R. & THOMAS, LEIF N. 2025 Refraction of near-inertial waves by submesoscale vorticity filaments. *Journal of Fluid Mechanics* **1020**, A9.

HOSKINS, B. J. & BRETHERTON, F. P. 1972 Atmospheric frontogenesis models: Mathematical formulation and solution. *Journal of Atmospheric Sciences* **29** (1), 11 – 37.

JOHNSON, LEAH & FOX-KEMPER, BAYLOR 2024 Modification of boundary layer turbulence by submesoscale flows. *Flow* **4**, E20.

KAFIABAD, HOSSEIN A., VANNESTE, JACQUES & YOUNG, WILLIAM R. 2021 Interaction of near-inertial waves with an anticyclonic vortex. *Journal of Physical Oceanography* **51** (6), 2035 – 2048.

KHATRI, HEMANT & BERLOFF, PAVEL 2018 A mechanism for jet drift over topography. *Journal of Fluid Mechanics* **845**, 392–416.

LEGAY, ALEXANDRE, DEREMBLE, BRUNO, PENDUFF, THIERRY, BRASSEUR, PIERRE & MOLINES, JEAN-MARC 2024 A framework for assessing ocean mixed layer depth evolution. *Journal of Advances in Modeling Earth Systems* **16** (10), e2023MS004198.

LÉVY, MARINA, FERRARI, RAFFAELE, FRANKS, PETER J. S., MARTIN, ADRIAN P. & RIVIÈRE, PASCAL 2012 Bringing physics to life at the submesoscale. *Geophysical Research Letters* **39** (14).

MAHADEVAN, AMALA 2016 The impact of submesoscale physics on primary productivity of plankton. *Annual Review of Marine Science* **8** (Volume 8, 2016), 161–184.

MAHADEVAN, A., TANDON, A. & FERRARI, R. 2010 Rapid changes in mixed layer stratification driven by submesoscale instabilities and winds. *Journal of Geophysical Research: Oceans* **115** (C3), arXiv: <https://agupubs.onlinelibrary.wiley.com/doi/pdf/10.1029/2008JC005203>.

MCWILLIAMS, JAMES C. 2016 Submesoscale currents in the ocean. *Proceedings of the Royal Society A: Mathematical, Physical and Engineering Sciences* **472** (2189), 20160117.

MCWILLIAMS, JAMES C. 2017 Submesoscale surface fronts and filaments: secondary circulation, buoyancy flux, and frontogenesis. *Journal of Fluid Mechanics* **823**, 391–432.

MCWILLIAMS, JAMES C., GRAVES, LEE P. & MONTGOMERY, MICHAEL T. 2003 A formal theory for vortex rossby waves and vortex evolution. *Geophysical & Astrophysical Fluid Dynamics* **97** (4), 275–309, arXiv: <https://doi.org/10.1080/0309192031000108698>.

PEREZHOGIN, PAVEL, ZHANG, CHENG, ADCROFT, ALISTAIR, FERNANDEZ-GRANDA, CARLOS & ZANNA, LAURE 2024 A stable implementation of a data-driven scale-aware mesoscale parameterization. *Journal of Advances in Modeling Earth Systems* **16** (10), e2023MS004104.

RAMADHAN, ALI, WAGNER, GREGORY LECLAIRE, HILL, CHRIS, CAMPIN, JEAN-MICHEL, CHURAVY, VALENTIN, BESARD, TIM, SOUZA, ANDRE, EDELMAN, ALAN, FERRARI, RAFFAELE & MARSHALL, JOHN 2020 Oceananigans.jl: Fast and friendly geophysical fluid dynamics on gpus. *Journal of Open Source Software* **5** (53), 2018.

SCOTT, RICHARD K. & DRITSCHEL, DAVID G. 2012 The structure of zonal jets in geostrophic turbulence. *Journal of Fluid Mechanics* **711**, 576–598.

SHAKESPEARE, CALLUM J. 2016 Curved density fronts: Cyclogeostrophic adjustment and frontogenesis. *Journal of Physical Oceanography* **46** (10), 3193 – 3207.

SHAKESPEARE, CALLUM J. & TAYLOR, J. R. 2013 A generalized mathematical model of geostrophic adjustment and frontogenesis: uniform potential vorticity. *Journal of Fluid Mechanics* **736**, 366–413.

SIEGELMAN, LIA, KLEIN, PATRICE, RIVIÈRE, PASCAL, THOMPSON, ANDREW F., TORRES, HECTOR S., FLEXAS, MAR & MENEMENLIS, DIMITRIS 2020 Enhanced upward heat transport at deep submesoscale ocean fronts. *Nature Geoscience* **13** (1), 50–55.

SILVESTRI, SIMONE, WAGNER, GREGORY L., CAMPIN, JEAN-MICHEL, CONSTANTINOU, NAVID C., HILL, CHRISTOPHER N., SOUZA, ANDRE & FERRARI, RAFFAELE 2024 A new weno-based momentum advection scheme for simulations of ocean mesoscale turbulence. *Journal of Advances in Modeling Earth Systems* **16** (7), e2023MS004130.

SILVESTRI, SIMONE, WAGNER, GREGORY L., CONSTANTINOU, NAVID C., HILL, CHRISTOPHER N., CAMPIN, JEAN-MICHEL, SOUZA, ANDRE N., BISHNU, SIDDHARTHA, CHURAVY, VALENTIN, MARSHALL, JOHN & FERRARI, RAFFAELE 2025 A gpu-based ocean dynamical core for routine mesoscale-resolving climate simulations. *Journal of Advances in Modeling Earth Systems* **17** (4), e2024MS004465, e2024MS004465 2024MS004465, arXiv: <https://agupubs.onlinelibrary.wiley.com/doi/pdf/10.1029/2024MS004465>.

SINHA, ANIRBAN, CALLIES, JÖRN & MENEMENLIS, DIMITRIS 2023 Do submesoscales affect the large-scale structure of the upper ocean? *Journal of Physical Oceanography* **53** (4), 1025 – 1040.

SKYLLINGSTAD, ERIC D., DUNCOMBE, JENESSA & SAMELSON, ROGER M. 2017 Baroclinic frontal instabilities and turbulent mixing in the surface boundary layer. part ii: Forced simulations. *Journal of Physical Oceanography* **47** (10), 2429 – 2454.

## Turbulent ocean front under strain

SRINIVASAN, KAUSHIK, BARKAN, ROY & McWILLIAMS, JAMES C. 2023 A forward energy flux at submesoscales driven by frontogenesis. *Journal of Physical Oceanography* **53** (1), 287 – 305.

SU, ZHAN, WANG, JINBO, KLEIN, PATRICE, THOMPSON, ANDREW F. & MENEMENLIS, DIMITRIS 2018 Ocean submesoscales as a key component of the global heat budget. *Nature Communications* **9** (1), 775.

SULLIVAN, PETER P. & McWILLIAMS, JAMES C. 2018 Frontogenesis and frontal arrest of a dense filament in the oceanic surface boundary layer. *Journal of Fluid Mechanics* **837**, 341–380.

TAYLOR, JOHN R. & THOMPSON, ANDREW F. 2023 Submesoscale dynamics in the upper ocean. *Annual Review of Fluid Mechanics* **55** (Volume 55, 2023), 103–127.

THOMAS, LEIF & FERRARI, RAFFAELE 2008 Friction, frontogenesis, and the stratification of the surface mixed layer. *Journal of Physical Oceanography* **38** (11), 2501 – 2518.

THOMAS, LEIF N. 2005 Destruction of potential vorticity by winds. *Journal of Physical Oceanography* **35** (12), 2457 – 2466.

THOMAS, LEIF N., TAYLOR, JOHN R., FERRARI, RAFFAELE & JOYCE, TERENCE M. 2013 Symmetric instability in the gulf stream. *Deep Sea Research Part II: Topical Studies in Oceanography* **91**, 96–110, subtropical Mode Water in the North Atlantic Ocean.

THORPE, S. A. 2005 *The Turbulent Ocean*. Cambridge University Press.

TREGUIER, A. M., DE BOYER MONTÉGUT, C., BOZEC, A., CHASSIGNET, E. P., FOX-KEMPER, B., McC. HOGG, A., IOVINO, D., KISS, A. E., LE SOMMER, J., LI, Y., LIN, P., LIQUE, C., LIU, H., SERAZIN, G., SIDORENKO, D., WANG, Q., XU, X. & YEAGER, S. 2023 The mixed-layer depth in the ocean model intercomparison project (omip): impact of resolving mesoscale eddies. *Geoscientific Model Development* **16** (13), 3849–3872.

VERMA, VICKY, PHAM, HIEU T. & SARKAR, SUTANU 2022 Interaction between upper-ocean submesoscale currents and convective turbulence. *Journal of Physical Oceanography* **52** (3), 437 – 458.

WAGNER, GREGORY LECLAIRE, HILLIER, ADELINE, CONSTANTINOU, NAVID C., SILVESTRI, SIMONE, SOUZA, ANDRE, BURNS, KEATON, HILL, CHRIS, CAMPIN, JEAN-MICHEL, MARSHALL, JOHN & FERRARI, RAFFAELE 2024 Formulation and calibration of catke, a one-equation parameterization for microscale ocean mixing, arXiv: 2306.13204.

WAGNER, G. L., SILVESTRI, S., CONSTANTINOU, N. C., RAMADHAN, A., CAMPIN, J.-M., HILL, C., CHOR, T., STRONG-WRIGHT, J., LEE, X. K., POULIN, F., SOUZA, A., BURNS, K. J., BISHNU, S., MARSHALL, J. & FERRARI, R. 2025 High-level, high-resolution ocean modeling at all scales with Oceananigans. *arXiv preprint* , arXiv: 2502.14148.

WENEGRAT, JACOB O. 2023 The current feedback on stress modifies the ekman buoyancy flux at fronts. *Journal of Physical Oceanography* **53** (12), 2737 – 2749.

YIM, EUNOK, STEGNER, ALEXANDRE & BILLANT, PAUL 2019 Stability criterion for the centrifugal instability of surface intensified anticyclones. *Journal of Physical Oceanography* **49** (3), 827 – 849.